



HAL
open science

Keck and Hubble Observations Show that MOA-2008-BLG-379Lb is a Super-Jupiter Orbiting an M Dwarf

David Bennett, Aparna Bhattacharya, Jean-Philippe Beaulieu, Naoki Koshimoto, Joshua Blackman, Ian Bond, Clément Ranc, Natalia Reksini, Sean Terry, Aikaterini Vandorou, et al.

► **To cite this version:**

David Bennett, Aparna Bhattacharya, Jean-Philippe Beaulieu, Naoki Koshimoto, Joshua Blackman, et al.. Keck and Hubble Observations Show that MOA-2008-BLG-379Lb is a Super-Jupiter Orbiting an M Dwarf. *The Astronomical Journal*, 2024, 168 (1), pp.15. 10.3847/1538-3881/ad4880 . hal-04789836

HAL Id: hal-04789836

<https://hal.science/hal-04789836v1>

Submitted on 20 Nov 2024

HAL is a multi-disciplinary open access archive for the deposit and dissemination of scientific research documents, whether they are published or not. The documents may come from teaching and research institutions in France or abroad, or from public or private research centers.

L'archive ouverte pluridisciplinaire **HAL**, est destinée au dépôt et à la diffusion de documents scientifiques de niveau recherche, publiés ou non, émanant des établissements d'enseignement et de recherche français ou étrangers, des laboratoires publics ou privés.



Distributed under a Creative Commons Attribution 4.0 International License



Keck and Hubble Observations Show that MOA-2008-BLG-379Lb is a Super-Jupiter Orbiting an M Dwarf

David P. Bennett^{1,2} , Aparna Bhattacharya^{1,2}, Jean-Philippe Beaulieu^{3,4} , Naoki Koshimoto^{1,2,5} , Joshua W. Blackman⁶ , Ian A. Bond⁷, Clément Ranc⁸ , Natalia Reksini^{3,4}, Sean K. Terry^{1,2,9} , Aikaterini Vandenrou^{1,2}, Jessica R. Lu⁹ ,

Jean Baptiste Marquette¹⁰, Greg Olmschenk^{1,2} , and Daisuke Suzuki⁵

¹ Code 667, NASA Goddard Space Flight Center, Greenbelt, MD 20771, USA; bennettd@umd.edu

² Department of Astronomy, University of Maryland, College Park, MD 20742, USA

³ School of Physical Sciences, University of Tasmania, Private Bag 37 Hobart, Tasmania 7001, Australia

⁴ Institut d'Astrophysique de Paris, 98 bis bd Arago, 75014 Paris, France

⁵ Department of Earth and Space Science, Graduate School of Science, Osaka University, Toyonaka, Osaka 560-0043, Japan

⁶ Physikalisches Institut, Universität Bern, Gessellschaftsstrasse 6, CH-3012 Bern, Switzerland

⁷ Institute of Natural and Mathematical Sciences, Massey University, Auckland 0745, New Zealand

⁸ Sorbonne Université, CNRS, Institut d'Astrophysique de Paris, IAP, F-75014 Paris, France

⁹ University of California Berkeley, Berkeley, CA, USA

¹⁰ Laboratoire d'astrophysique de Bordeaux, Univ. Bordeaux, CNRS, B18N, allée Geoffroy Saint-Hilaire, 33615 Pessac, France

Received 2023 November 1; revised 2024 April 22; accepted 2024 May 5; published 2024 June 18

Abstract

We present high angular resolution imaging that detects the MOA-2008-BLG-379L exoplanet host star using Keck adaptive optics and the Hubble Space Telescope. These observations reveal host star and planet masses of $M_{\text{host}} = 0.434 \pm 0.065 M_{\odot}$ and $m_p = 2.44 \pm 0.49 M_{\text{Jupiter}}$. They are located at a distance of $D_L = 3.44 \pm 0.53$ kpc, with a projected separation of 2.70 ± 0.42 au. These results contribute to our determination of exoplanet host star masses for the Suzuki et al. statistical sample, which will determine the dependence of the planet occurrence rate on the mass and distance of the host stars. We also present a detailed discussion of the image-constrained modeling version of the `eSunhong` light-curve modeling code that applies high angular resolution image constraints to the light-curve modeling process. This code increases modeling efficiency by a large factor by excluding models that are inconsistent with the high angular resolution images. The analysis of this and other events from the Suzuki et al. statistical sample reveals the importance of including higher-order effects, such as microlensing parallax and planetary orbital motion, even when these features are not required to fit the light-curve data. The inclusion of these effects may be needed to obtain accurate estimates of the uncertainty of other microlensing parameters that affect the inferred properties of exoplanet microlens systems. This will be important for the exoplanet microlensing survey of the Roman Space Telescope, which will use both light-curve photometry and high angular resolution imaging to characterize planetary microlens systems.

Unified Astronomy Thesaurus concepts: [Gravitational microlensing exoplanet detection \(2147\)](#); [Extrasolar gaseous giant planets \(509\)](#); [Galactic bulge \(2041\)](#); [Adaptive optics \(2281\)](#); [Hubble Space Telescope \(761\)](#)

1. Introduction

Gravitational microlensing surveys of the Galactic bulge have long been recognized as an effective way (Mao & Paczynski 1991) to discover exoplanets down to low masses (Bennett & Rhie 1996) orbiting beyond the snow line (Gould & Loeb 1992). Because of this, the Astro2010 decadal survey recommended a space-based exoplanet microlensing survey (Bennett & Rhie 2002; Bennett et al. 2010a; Spergel et al. 2015; Penny et al. 2019) to complete the statistical census of exoplanets in orbits $\gtrsim 1$ au to complement Kepler's survey of planets in short-period orbits (Thompson et al. 2018).

Previous statistical studies of planetary microlensing events have revealed that super-Earths and Neptunes are more common than higher-mass planets (Gould et al. 2006, 2010; Sumi et al. 2010; Cassan et al. 2012; Suzuki et al. 2016). The largest microlensing sample analyzed to date (Suzuki et al. 2016, 2018) has revealed a contradiction to a prediction based on the leading core accretion theory of planet formation

(Lissauer 1993; Pollack et al. 1996). The standard core accretion theory includes a runaway gas accretion process, in which giant planet cores of $\sim 10 M_{\oplus}$ grow rapidly to masses similar to that of Jupiter ($318 M_{\oplus}$) by accretion of hydrogen and helium gas. This process led to predictions (Ida & Lin 2004; Mordasini et al. 2009; Emsenhuber et al. 2021) of a sub-Saturn mass “desert” in the distribution of exoplanets because it was thought to be very unlikely for gas accretion to terminate in the middle of this rapid growth phase. However, the Microlensing Observations in Astrophysics (MOA) Collaboration microlensing results (Suzuki et al. 2016) indicated a smooth, power-law distribution through this sub-Saturn mass region, in contradiction to these earlier theoretical predictions (Suzuki et al. 2018), although more sophisticated theoretical calculations do predict a power-law mass function down to mass ratios of $\sim 10^{-4}$ (Adams et al. 2021). In addition, a rigorous reanalysis of the Mayor et al. (2011) radial velocity exoplanet sample indicated no evidence for such a desert (Bennett et al. 2021), despite suggestions to the contrary in the Mayor et al. (2011) paper. The more recent radial velocity results from the California Legacy Survey (Fulton et al. 2021; Rosenthal et al. 2021) also show no evidence for such a sub-Saturn mass exoplanet desert. These observations are consistent



Original content from this work may be used under the terms of the [Creative Commons Attribution 4.0 licence](#). Any further distribution of this work must maintain attribution to the author(s) and the title of the work, journal citation and DOI.

with three-dimensional hydrodynamic simulations that show that the formation of a circumplanetary disk can slow gas accretion (Szulágyi et al. 2014) and that the gas accretion can also be slowed by collisions of protoplanets (Ali-Dib et al. 2022). Atacama Large Millimeter/submillimeter Array observations of gaps in protoplanetary disks are also easier to explain (Nayakshin et al. 2019, 2022) with giant planet growth that is slower than predicted by the runaway accretion scenario.

One characteristic of the exoplanets beyond the snow line found by microlensing that has not been explored is the dependence of the planet occurrence rate, as a function of host mass, or more simply, the planet hosting probability as a function of host mass. Kepler data have demonstrated a dramatic difference in the planetary systems orbiting M dwarfs and those orbiting more solar-like stars of spectral types F, G, and K (Mulders et al. 2015). M dwarfs host many more small planets in short-period orbits than more massive host stars do. A different trend is expected for planets in wider orbits, beyond the snow line. It is expected that gas giant planets will form more easily around more massive stars (Laughlin et al. 2004) and that the protoplanetary disks of M dwarfs will often lose their hydrogen and helium gas before large amounts of gas can be accreted onto protoplanets. Microlensing has previously made mass measurements for two microlens planets with masses of $\sim 3 M_{\text{Jupiter}}$ orbiting M dwarfs of mass $\sim 0.43 M_{\odot}$ (Dong et al. 2009b; Poleski et al. 2014; Tsapras et al. 2014; Bennett et al. 2020), and in this paper, we present mass measurements of the MOA-2008-BLG-379Lb planet and host star masses very similar to these previous examples. This suggests that the formation of super-Jupiter mass planets orbiting M dwarf hosts is not as difficult as these theoretical predictions indicate, a feature that has also been seen in radial velocity studies (Schlecker et al. 2022). Perhaps this is not surprising given that the Laughlin et al. (2004) prediction is based on the runaway gas accretion process that also predicted the sub-Saturn mass “desert,” which is contradicted by the microlensing and radial velocity data. A statistical analysis of a sample of events with mass measurements is necessary for a definitive test of these predictions, and both the MOA-2008-BLG-379Lb and OGLE-2005-BLG-071Lb planets are part of the Suzuki et al. (2016) statistical sample that we are obtaining mass measurements for. However, preliminary analyses of both this Suzuki et al. (2016) microlensing sample and the California Legacy Survey radial velocity sample (Fulton et al. 2021; Rosenthal et al. 2021) indicate that the exoplanet hosting probability for wide-orbit planets scales as roughly the first power of the host star mass.¹¹

It is also thought that wide-orbit planets ranging in mass from $\sim 10 M_{\oplus}$ to a few Jupiter masses may be needed (Raymond et al. 2004, 2007; Childs et al. 2022) to create habitable conditions on terrestrial planets in inner orbits. These wide-orbit planets are expected to be crucial for the delivery of water and other ingredients that may be needed for life to develop on these potentially habitable planets (Grazier 2016; Osinski et al. 2020; Sinclair et al. 2020). Thus, an understanding of the host mass dependence of planets found by microlensing may help us gain an understanding of which planetary systems might include habitable planets. The planetary system we study in this paper has a mass ratio of $\sim 5 \times 10^{-3}$, which would indicate a super-Jupiter mass planet

orbiting an M dwarf if the host mass is in the range $0.19 < M_{\text{host}}/M_{\odot} < 0.6$, which is, in fact, what we find.

In this paper, we use adaptive optics (AO) observations with the NIRC2 instrument on the Keck II telescope and Hubble Space Telescope observations to identify the lens and planetary host star and provide a precise measurement of the masses and distance of the MOA-2008-BLG-379L planetary system.

This paper is organized as follows. In Section 2 we present the light curve of microlensing event MOA-2008-BLG-379 and explain the challenges posed by the faintness of its source star. In Section 3, we describe the Hubble Space Telescope and Keck high angular resolution follow-up observations and their analysis. Section 4.3 presents a new method to apply the constraints from high angular resolution to the light-curve modeling analysis. The constraints from the light-curve models and high angular resolution follow-up observations are combined with relatively weak constraints from a Galactic model to derive the physical properties of the MOA-2008-BLG-379Lb planetary system in Section 5, and then in Section 6 we describe the implications of our high angular resolution imaging program for the Roman Galactic Exoplanet Survey. We discuss the implications of these results and present our conclusions in Section 7, and the Appendix compares the light-curve model presented by Suzuki et al. (2014a, 2014b) with models using the *eesunhong* code and with improved MOA photometry.

2. Microlensing Event MOA-2008-BLG-379

MOA-2008-BLG-379 (Suzuki et al. 2014a, 2014b), located at (R.A., decl.) (J2000) = (17^h58^m49^s.44, -30°11′48″.95), is an unusual planetary microlensing event in that, despite a very strong planetary signal, it was not identified as a planetary microlensing event until several years after it was observed, even though the light-curve photometry from the MOA and Optical Gravitational Lensing Experiment (OGLE) groups could be viewed on the microlensing alert websites very shortly after the data were taken. The event was first discovered by the MOA alert system (Bond et al. 2001) at UT 22:00, 2008 August 9 (or or HJD’ = HJD - 2,450,000 = 4688.42). The data taken on the next night revealed a strong caustic entry feature that make it clear that this was not a single-lens microlensing event, and data from the OGLE group soon confirmed this conclusion when they independently discovered the event two weeks later. (The OGLE discovery was delayed because it was found during the development of the “new object” channel of the OGLE Early Warning System (Udalski et al. 1994) that could find microlensing events, like MOA-2008-BLG-379, with faint source stars that were not close to an apparent “star” identified in the OGLE reference image.)

While the light curve, shown in Figure 1, was clearly not that of a single-lens event, it was observed at a time when only seven planetary microlensing events had been published (Bond et al. 2004; Udalski et al. 2005; Beaulieu et al. 2006; Gould et al. 2006; Gaudi et al. 2008; Bennett et al. 2008) and three more were well known to the microlensing community while under analysis (Dong et al. 2009a; Sumi et al. 2010; Bennett et al. 2016). MOA-2008-BLG-379 showed dramatic deviations from a single-lens light curve over about half of its apparent duration, and it was not immediately recognized that an event like this could be due to very high magnification by a planetary lens system with a very faint source star. The faintness of the source star meant that much of the lower-magnification part of the light curve did not rise above the photometric noise.

¹¹ <https://clementranc.github.io/microlensing25/schedule/talks/bendav.html>

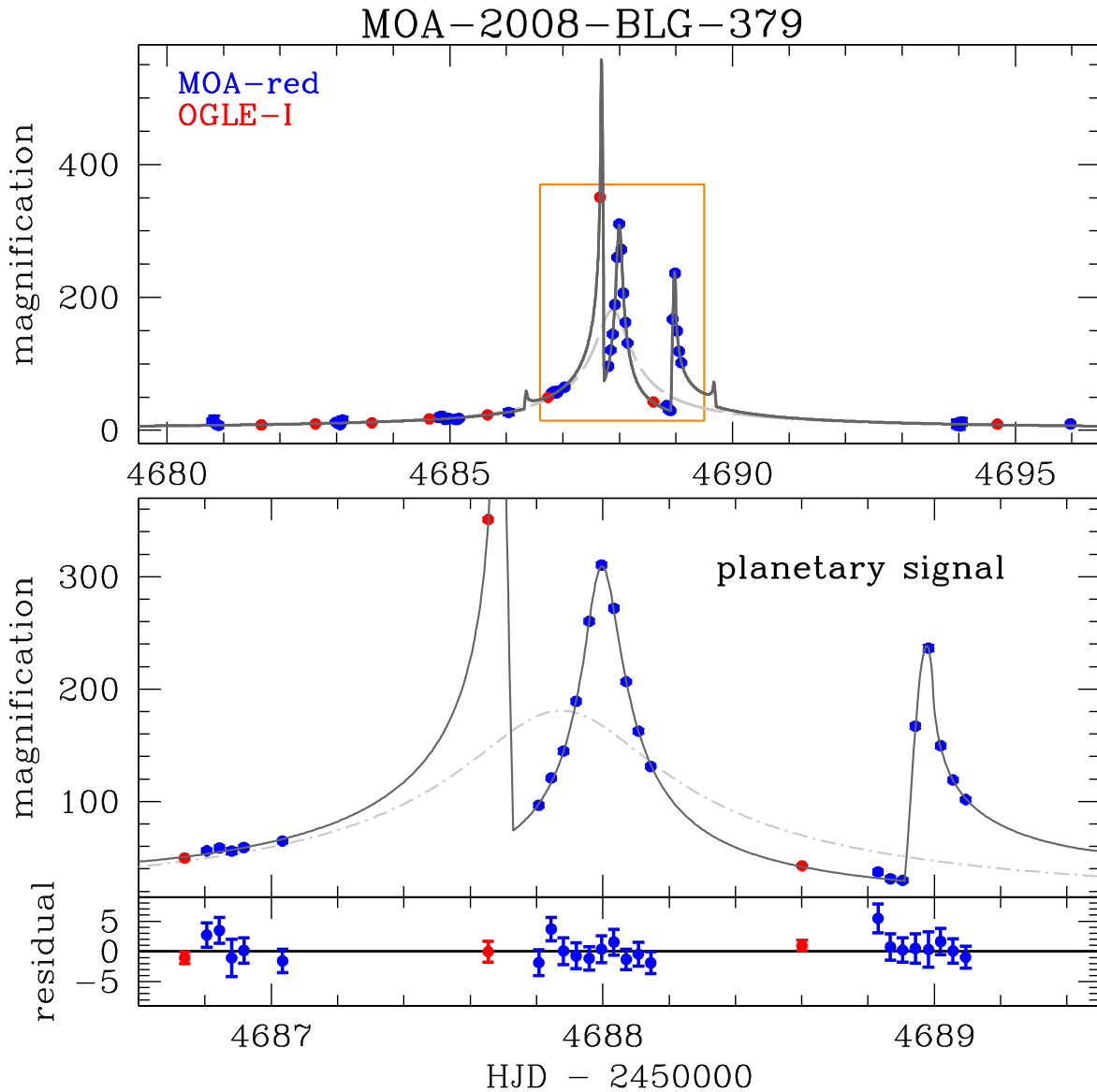


Figure 1. The best-fit light curve with the constraints from the high angular resolution follow-up data, as explained in Section 4.3. This is the model from the third column of Table 3, with $u_0 > 0$ and $s > 1$.

The planetary nature of this event was discovered several years later as a part of the statistical analysis that led to the MOA Collaboration study of exoplanet demographics beyond the snow line (Suzuki et al. 2016). It is now generally understood that a light curve like the one shown in Figure 1 can only be explained by a microlensing model with a planetary mass ratio below the International Astronomical Union preferred mass ratio threshold of $q < 0.0400642$ (Lecavelier des Etangs & Lissauer 2022).

While the planetary nature of the light curve is clear, there is an additional complication due to the faint source star. This is due to the formula for microlensing magnification by a single, compact lens, $A = (u^2 + 2)/(u\sqrt{u^2 + 4})$, where u is the lens-source separation in units of the Einstein radius. As a single-lens approaches high magnification, the lens-source alignment becomes nearly perfect, so that $u \rightarrow 0$. In this limit, we have $A \approx 1/u$, so that the apparent brightness becomes $F_{s,\text{obs}} \approx F_s/u$, where $F_{s,\text{obs}}$ and F_s are the magnified and unlensed brightnesses of the background source, respectively. This is a

difficulty because main-sequence stars are not individually resolved in ground-based observations of the crowded Galactic bulge fields, where most gravitational microlensing events are observed. Thus, the brightness of the source star is normally determined from the light-curve model fit, but this can be a problem for high-magnification microlensing events. When the high-magnification approximation, $F_{s,\text{obs}} \approx F_s/u$, applies, the light-curve shape will only reveal the combination F_s/u , but not F_s and u individually. Thus, F_s can only be determined from the lower-magnification parts of the light curve, where the high-magnification approximation does not apply. When the source star is faint, this becomes difficult and sensitive to low-level light-curve systematic errors, so the faintness of the MOA-2008-BLG-379 source implies that the light-curve modeling will result in imprecise measurements of t_E and F_s . Both of these parameters are used in the mass and distance determination for the lens system, so this is an important part of the rationale for the new modeling code that we discuss in Section 4.3. This new code applies the constraints from the high angular resolution images to the light-curve models.

We have used an improved data reduction method using the difference imaging code of Bond et al. (2001), but we have applied the detrending method of Bond et al. (2017) to remove systematic errors, including the color-dependent effects of differential refraction (Bennett et al. 2012) that are enhanced by the wide MOA-red passband used for the MOA II survey. This method also calibrates the MOA data to the OGLE III catalog (Szymański et al. 2011). However, since no MOA V -band data were taken in 2008, we must use a $V-I$ color from other observations to relate the MOA-red magnitude to the I band. We find

$$I = R_{\text{MOA}} + 28.1940 - 0.2002(V - I), \quad (1)$$

where the MOA-red magnitude, R_{MOA} , is related to the MOA instrumental flux units, F_{MOA} , by $R_{\text{MOA}} = -2.5 \log_{10}(F_{\text{MOA}})$. We will use the Hubble observations to help determine the $V-I$ color of the source star.

3. Hubble Space Telescope and Keck Follow-up Observations and Analysis

The first high angular resolution follow-up observations for MOA-2008-BLG-379 were taken by Hubble on 2013 October 9, which was shortly after the planetary nature of the event was discovered and before the planetary discovery paper was published (Suzuki et al. 2014a, 2014b). Hubble Space Telescope program GO-12541 had already been approved for two epochs of follow-up observations of four other planetary microlensing events. However, the first epoch observations of OGLE-2005-BLG-169 were sufficient to determine the physical parameters of this event (Bennett et al. 2015), particularly when combined with a later epoch of Keck telescope AO imaging (Batista et al. 2015). Thus, we were able to switch the target for these second epoch observations from OGLE-2005-BLG-169 to the event we analyze in this paper, MOA-2008-BLG-379. We obtained 16 Hubble Wide Field Camera 3 UVIS images of this event with 8×70 s and 8×125 s dithered exposures in the F814W and F555W passbands, respectively. However, the MOA-2008-BLG-379 source star is a magnitude fainter than the OGLE-2005-BLG-169, so we probably would have asked for observations using two instead of one Hubble orbit if we had originally proposed to observe the MOA-2008-BLG-379 event. As a result, the signal-to-noise ratio of the Hubble data was lower than desired, and our initial analysis did not separately detect the source and lens stars.

The Hubble data used in this paper can be found at doi:10.17909/edn8-2564. The Keck data for the May, 2018 observations can be found at <http://dx.doi.org/10.26135/KOA3>, and <http://dx.doi.org/10.17909/edn8-2564> contains the August, 2018 data. Note that DOIs for the Keck observations link to observations of many events. Filter for the observations used in this paper with the target name mb08379.

3.1. Keck Data Analysis

Because of the low signal-to-noise ratio of the Hubble data, we also observed this event in 2018 as a part of our NASA Keck Key Strategic Mission Support “Development of the WFIRST Exoplanet Mass Measurement Method,” using the laser guide star AO mode of the NIRC2 instrument with the K_s filter on the Keck II telescope. In order to calibrate the Keck photometry, we obtained 10 images with 30 s exposures using the NIRC2 wide camera on 2018 May 27. The wide camera images cover a

1024×1024 pixel area with a plate scale of 39.686 mas per pixel. We adopted a 5 points dither pattern with a step of $2''$ for the 10 images. These K_s wide camera images were flat field and dark current corrected using standard methods (Batista et al. 2014; Beaulieu et al. 2016); then we performed the sky correction and stacked the images using the SWarp Astrometrics package (Bertin et al. 2002). We used the SExtractor (Bertin & Arnouts 1996) package to obtain photometry with a 10 pixel aperture. We cross-identified the detected sources with our rereduction of K -band images from the Vista VVV survey (Minniti et al. 2010) as described by Beaulieu (2018). We select 39 cross-identified stars to obtain the zero point for the Keck photometry. We then obtained the measured flux of the combined lens plus source (or stars 1 + 2) images to be $K_{s12} = 18.09 \pm 0.05$, with a calibration error of 2%.

The detailed analysis of the blended background source star and foreground lens (and planetary host) star requires higher angular resolution than the NIRC2 wide camera provides, so the NIRC2 narrow camera was used. The NIRC2 narrow camera uses the same 1024×1024 pixel detector as the wide camera, but the plate scale is $4 \times$ smaller at 9.942 mas per pixel. The first set of NIRC2 narrow camera images of our target were taken on 2018 May 26 with a small dither pattern and each of 18 frames consisting of two coadded 30 s exposures. Another set of 17 frames, each consisting of three coadded 20 s exposures, were taken on 2018 August 6, with a similar small dither pattern. All images were taken with the K_s filter.

The images taken in May and August were analyzed separately. The raw images were flat fielded and bias subtracted, and then bad pixels and cosmic rays were removed from the raw images. Then these cleaned raw images were corrected for geometric distortion and differential atmospheric refraction and stacked into a single coadded frame for each of the May and August data sets using the methods of Lu (2008, 2022). This process also resulted in the removal of a few lower-quality images from each of the May and August data sets. The images included in these final stacked images had mean and rms point-spread function (PSF) FWHM values of $\text{FWHM} = 71.5 \pm 2.8$ mas for the 13 good images from the May data set and $\text{FWHM} = 58.6 \pm 4.4$ mas for the 12 good images from the August data set. Figure 2(a) shows the stacked NIRC2 narrow camera image from 2018 August, and Figure 2(b) shows a close-up image, approximately 250 mas on a side at the location of the MOA-2008-BLG-379 microlensing event. This event involved stars 1 and 2, which we will identify as the lens and source stars with the help of the earlier Hubble images.

We have analyzed these coadded NIRC2 narrow camera images following the method of Bhattacharya et al. (2018) using DAOPHOT (Stetson 1987). The DAOPHOT PSF models were built in two stages. First, we ran DAOPHOT’s FIND and PHOT commands to find all the stars in the image, and then we used the DAOPHOT PICK command to build a list of bright ($K_s < 18.5$) isolated stars that can be used to construct our empirical PSF models. Our target “star” is actually bright enough to pass this magnitude cut, but by 2018 the images of the two stars had separated enough to be resolved and both stars were fainter than $K_s = 18.5$. However, our analysis must always exclude the target from the candidate PSF star list because it must necessarily consist of the lens and source stars separating after the microlensing event. The PSF stars were selected to be located close to the target, with a roughly even

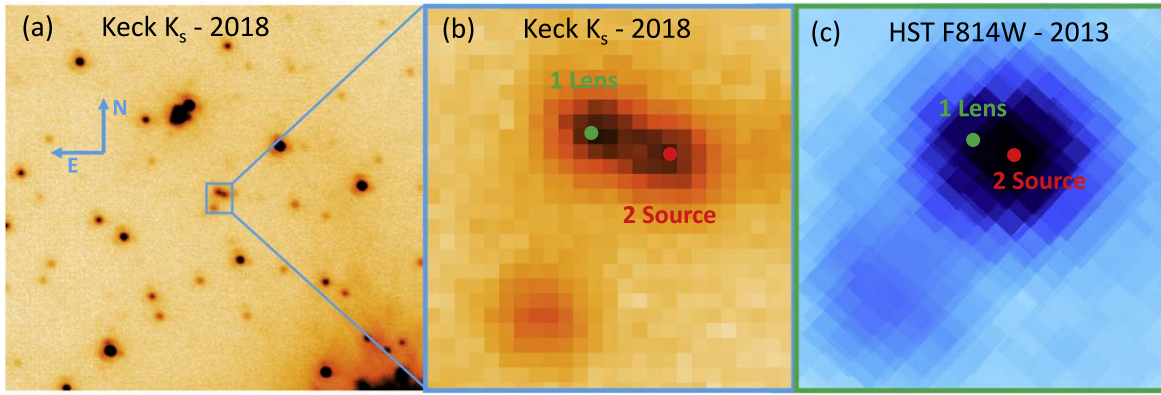


Figure 2. (a) A $32'' \times 32''$ section of the coadded sum of 12×60 s exposures with the Keck NIRC2 narrow camera images taken 10 years after the microlensing event, with the target location indicated by a blue square. The images in panels (b) and (c) are $2.5'' \times 2.6''$ close-ups of the target with the Keck K_s band and the Hubble WFC3/UVIS F814W passband, respectively. The green and red dots are the best-fit positions of the lens and source stars. The coadded Hubble frame, taken in 2013, involves no image resampling. Instead, each pixel of the individual Hubble images is divided into 100×100 subpixels, which are each assigned the same flux value. Thus, image (c) shows full-size pixels with the observed dither offsets accurate to 0.01 pixels.

Table 1
Keck NIRC2 Narrow Camera Fit Parameters

Data Set	$K_{s1} - K_{s2}$	R.A. ₁ - R.A. ₂ (mas)	Decl. ₁ - Decl. ₂ (mas)
2018 May	-0.2058 ± 0.0661	55.91 ± 1.55	18.57 ± 0.80
2018 Aug	-0.0325 ± 0.0264	53.79 ± 0.69	19.44 ± 0.44
Weighted sum	-0.0564 ± 0.0245	54.14 ± 0.63	19.24 ± 0.38
		$\mu_{\text{rel,H,E}}(\text{mas yr}^{-1})$	$\mu_{\text{rel,H,N}}(\text{mas yr}^{-1})$
		5.430 ± 0.063	1.926 ± 0.038

Note. The separation was measured by Keck K -band images taken 9.9900 years after the peak of the event. The follow-up observation was taken on 2018 August 6, and the peak of the microlensing light-curve event was on 2008 August 9.

distribution on all sides of the target to minimize any effects of a spatially varying PSF.

Once we have built the PSF model for each coadded frame, we use DAOPHOT’s ALLSTAR routine to fit all the stars in the image, including the lens and source star pair that are shown in panels (a) and (b) of Figure 2. The locations of the source and lens stars were determined with the standard method using difference images taken near peak magnification (Bennett et al. 2006, 2010b; Sumi et al. 2010), which are then transformed to the NIRC2 wide camera image, which has been astrometrically matched to the coordinate system of the MOA reference image.

The error bars are determined with the jackknife method (Quenouille 1949, 1956; Tukey 1958; Tierney & Mira 1999) following Bhattacharya et al. (2021). This method is able to determine uncertainties due to the PSF variations in the individual images. For the May data, the jackknife method requires that $N=13$ different “jackknife” coadded images are constructed, with each of the 13 good May images being excluded from one of these jackknife images. These images are all then analyzed with same dual-star PSF models as the full combined image of all 13 good images, yielding 13 sets of dual-star fit parameters. We use the mean of these parameters in these jackknife reductions as our best-fit parameters, shown in Table 1, with the uncertainty for a parameter, x , given by the jackknife formula,

$$\sigma_x = \sqrt{\frac{N-1}{N} \sum (x_i - \bar{x})^2}, \quad (2)$$

where x_i is the parameter value from the i th jackknife image stack and \bar{x} is the mean value of the parameter from the jackknife images. This Equation (2) is the same formula as the sample mean error, except that it is multiplied by $\sqrt{N-1}$ to account for the fact that each individual image is included in all but one of the jackknife image stacks. The August data are reduced in the same way, except that the number of good images is $N=12$.

The results of our analysis are summarized in Table 1, which shows the magnitude difference and separation measurements from the May and August Keck reductions. The reported values are the mean of the measurements from the jackknife runs, and the error bars are determined from Equation (2). The August data have a smaller scatter than the May data due to somewhat distorted PSF shapes in the May data. The third line of Table 1 shows the weighted sum of these measurements, and it appears that the May measurement of the magnitude difference is more than 2σ larger than the weighted sum of the magnitude difference. However, we should note that there are only 13 images that contribute to the jackknife error bars, so the precision of the error bar estimates is subject to a Poisson uncertainty of $\sim 1/\sqrt{13} = 28\%$. Thus, a 1σ increase in the error bar would bring the magnitude difference from May to within 2σ of the weighted average value. We will use the weighted sum values for the remainder of our analysis. The magnitude of the lens–source relative proper motion in the heliocentric frame is $\mu_{\text{rel,H}} = 5.761 \pm 0.061 \text{ yr}^{-1}$.

Since the magnitude difference of the two stars is only $K_{s1} - K_{s2} = -0.0564 \pm 0.0245$, we cannot use the estimated K_s

Table 2
Hubble Multistar PSF Fit Results

Filter	$\mu_{\text{rel,H}}$ const.	x_{hst1} (pix) Star 1 = Lens	y_{hst1} (pix)	x_{hst2} (pix) Star 2 = Source	y_{hst2} (pix)	F_{hst1} (Lens)	F_{hst2} (Source)
F814W	yes	-0.513(78)	-0.206(42)	0.171(74)	0.100(73)	316(133)	941(128)
F814W	no	-0.389(116)	-0.242(84)	0.168(60)	0.139(47)	389(136)	867(135)
F555W	yes	-0.524(47)	-0.235(37)	0.164(74)	0.061(28)	50(42)	680(38)
F555W	yes	0.769(43)	0.329(32)	0.081(37)	0.028(24)	55(38)	677(33)

Note. The coordinate system used here is centered on the center of the blended image of stars 1 and 2 in a preliminary reduction of an F814W that was arbitrarily selected as the reference frame.

magnitude of the source star from the light-curve model to determine which star is the source star to high confidence. This is why we label the stars with numbers 1 and 2, in addition to the lens and the source. While the Keck observations do not allow us to determine which of stars 1 and 2 is the source star, we will see in Section 3.2 that our earlier, 2013, Hubble observations will answer this question. With the calibration of the combined stars 1 + 2 flux from the NIRC2 wide camera, we have $K_{s1} = 18.815 \pm 0.056$ and $K_{s2} = 18.871 \pm 0.056$.

3.2. Hubble Data Analysis

As mentioned in the introduction to Section 3, we obtained a single orbit of Hubble observations from program GO-13417, using the WFC3/UVIS camera, in 2013, five years after the event. We obtained 8×70 s dithered exposures with the F814W filter and 8×70 s dithered exposures with the F555W filter using the UVIS2-C1K1C-SUB aperture to minimize Charfe Transfer Efficiency (CTE) losses and minimize readout times in order to obtain 16 dithered images in a single orbit. (The Hubble data used in this paper can be found in *Mikulski Archive for Space Telescopes* (MAST) doi: [10.17909/edn8-2564](https://doi.org/10.17909/edn8-2564).) The analysis was done with a modified version of the codes used by Bennett et al. (2015) and Bhattacharya et al. (2018), and these codes analyze the data from the original images without any resampling in order to avoid the loss of resolution that the combination of dithered, undersampled images would provide. Figure 2(c) shows a close-up of the eight dithered F814W images registered to the same physical coordinate system plotted on top of each other. This is a representation of the data that our analysis code uses, because we simultaneously analyze the eight individual images with pixel positions transformed to the same physical coordinate system. Because the Hubble and Keck images were taken 5.1657 and 9.9900 yr after the event, respectively, the Hubble images should show a lens–source separation that is about a factor of 2 smaller than the separation seen in the Keck image. The angular resolution of the Hubble images is also worse than the angular resolution of the Keck images because of Hubble’s smaller aperture and relatively large undersampled pixels. (However, the much more stable PSF shapes delivered by Hubble help to compensate for the lower angular resolution in this type of analysis.)

With the lower angular resolution of the Hubble images, we had some concern that the image of the fainter star to the southwest of the lens and source might interfere with the measurement of the lens–source separation, so we have included this third star in our PSF fitting procedure. Also, the Keck data provide a higher signal-to-noise ratio measurement of the two-dimensional separation between the lens and source stars, so we have added the option of applying a constraint to

the two-dimensional separation of stars 1 and 2 in our three-star Hubble PSF fitting code. Because the Hubble images were obtained earlier than the Keck images, the separation of the lens and source star should be $0.51709 \times$ smaller in the Hubble images than in the Keck images.

The coordinate transformation between the Keck and Hubble images was done with 17 stars brighter than $K_s < 14.8$, yielding the transformation

$$\begin{aligned} x_{\text{hst}} &= 0.184169 x_{\text{keck}} - 0.171462 y_{\text{keck}} + 483.4065, \\ y_{\text{hst}} &= 0.171174 x_{\text{keck}} + 0.183673 y_{\text{keck}} + 399.7104, \end{aligned} \quad (3)$$

from Keck to Hubble WFC3/UVIS pixels. The rms scatter for this relation is $\sigma_x = 0.33$ and $\sigma_y = 0.28$ WFC3/UVIS pixels for the 17 stars used for the transformation. The Keck images were taken 5 years after the Hubble images, and the WFC3/UVIS pixels subtend 40 mas. Thus, the ~ 12 mas scatter in the x and y coordinates could be fully explained by an average proper motion of 2.4 mas per year in each direction. This magnitude of proper motion is typical of bulge stars, so it seems likely that the scatter is largely explained by stellar proper motion of the astrometric reference stars.

Equation (3) allows us to convert the Keck relative proper motion values ($\mu_{\text{rel,H}}$) given at the bottom of Table 1 to constraints on the positions of the source and lens stars in the Hubble images, taking into account the 5.1657 yr interval between the microlensing event peak and the Hubble observations. Table 2 shows the the positions and instrumental fluxes of the two stars of interest from our constrained and unconstrained three-star PSF fitting procedure. (The third star is included in the fit to prevent it from biasing the measurements of the lens and source stars.) As we shall see below, these results allow us to identify star 1 as the lens (and planetary host) star and star 2 as the source star. The instrumental fluxes of stars 1 and 2 in Figure 2(c) are denoted by F_{hst1} and F_{hst2} , and the two- or three-digit numbers given in parentheses are the uncertainties of the last two or three decimal places for each measurement. We have analyzed the Hubble F814W data both with and without this proper motion constraint, but the F555W images can detect the fainter star at only 1σ precision, so we have only done constrained fits for this passband. The rows shown in boldface are the ones used for our final analysis.

The F814W fits converged to a unique solution with star 2, to the southeast, as the brighter star, but the F555W fits with a constraint on $\mu_{\text{rel,H}}$ were fit almost equally well with star 1 or star 2 being the brighter star, which is not a surprise, since the fainter star is $< 1.5\sigma$ from zero flux. Our reduction code puts the F814W and F555W coordinates in the same reference frame, so each star should have positions that are consistent between the two passbands. The F555W model highlighted in

boldface gives positions for stars 1 and 2 that are consistent with the positions listed in the first F814W row (also highlighted in boldface). The measurements from these rows can be averaged to find the weighted mean positions, and this yields average positions for both stars of $\chi^2 = 1.80$ for the eight measurements (two coordinates for each star in each passband), four parameters (the mean x and y values for each star), with two constraints (the separations implied by the $\mu_{\text{rel,H}}$ measurement). Thus, we have $\chi^2/\text{dof} = 0.30$. In the F555W model listed in the bottom row, we also label the brighter star to be star 2, but now star 1 is located in the opposite direction—to the northwest of star 2. The star 2 position is still marginally consistent with the F814W star 2 position, but the star 1 positions are pretty far from each other. The fit to average star 2 position using this bottom gives $\chi^2 = 3.83$, but the fit for the mean star 1 position gives $\chi^2 = 308.82$, so we have rejected this alternative F555W PSF fit model.

The Hubble data were calibrated to the OGLE III catalog (Szymański et al. 2011) using seven relatively bright OGLE III stars that were matched to isolated stars in the Hubble catalog. These calibrations give $I_2 = 21.56 \pm 0.15$, $V_2 = 23.67 \pm 0.06$, $I_1 = 22.75 \pm 0.49$, and $V_1 = 26.49^{+1.93}_{-0.66}$. As indicated in Table 2, the V -band (F555W) brightness of star 1 is very marginally detected at $\sim 1\sigma$ significance. The relatively large I -band uncertainties are largely due to the small lens–source separation of ~ 0.74 pixels, which allows flux to be traded between the two stars (Bennett et al. 2007). As a result, the magnitude of both the lens and source stars combined is measured with higher precision. We find the magnitude of the combination of stars 1 and 2 is $I_{12} = 21.250 \pm 0.011$.

With these V - and I -band measurements, we can now determine which star is the source and which is the lens. The discovery paper (Suzuki et al. 2014a, 2014b) determined the source star I magnitude to be $I_S = 21.30 \pm 0.03$ with a color of $V_S - I_S = 2.29 \pm 0.14$. However, since that analysis, the MOA group has begun detrending its photometry to remove systematic errors caused by the apparent motion of nearby stars of different colors due to atmospheric refraction. We used the detrending method of Bond et al. (2017) to correct these data and following Suzuki et al. (2014a, 2014b) excluded the data points that obtained prior to 2008 March 17 and after 2008 October 22. This analysis yielded a best-fit source magnitude of $I_S = 21.40$, which is just over 1σ brighter than the Hubble I -band magnitude for star 2 and is much brighter than Hubble I brightness of star 1. However, the detrending method of Bennett et al. (2012), which is less aggressive at removing trends due to variations in seeing, yielded predicted source brightnesses of $I_S \lesssim 21.0$. The best-fit models with longer durations of MOA data yielded even brighter source stars, and the exclusion of baseline observations with high air mass and poor seeing did not bring the best-fit source magnitude any closer to the Hubble values. This uncertainty in the source brightness is due to the fact that it is only the low-magnification part of the light curve that constrains the Einstein radius crossing time, t_E , and the source brightness. Thus, high-magnification events with faint sources, like MOA-2008-BLG-379, are susceptible to low-level systematic errors that can perturb the correct t_E and I_S values. This is sometimes referred to as the blending degeneracy (Di Stefano & Esin 1995; Alard 1997). Nevertheless, the light-curve data clearly favor the identification of star 2 as the source star. In contrast, the

$I_1 = 22.75 \pm 0.49$ mag is considerably fainter than the light-curve models predict.

The color of star 2, $V_2 - I_2 = 2.11 \pm 0.16$, also matches the Suzuki et al. (2014a, 2014b) color prediction of $V_S - I_S = 2.29 \pm 0.14$, and this color measurement is not affected by the blending degeneracy. The measured V_1 magnitude is quite uncertain, since the detection of this star is very marginal in the V band. The best-fit color for star 1 is $V_1 - I_1 = 3.74$, and even if we take the 2σ upper limit on the star 1 V -band brightness from Table 2, we have $V_1 - I_1 = 2.68$, which is still considerably redder than the source color from the light-curve models. So we identify star 2 to be the source star and star 1 to be the lens and planetary host star, as we have labeled in Figure 2. With the identification of star 1 with the lens star, the direction of motion of the lens star with respect to the source star is $\sim 40^\circ$ from the direction rotation of the Galactic disk. Since the disk rotation is a substantial fraction of the total velocity difference between disk and bulge stars, this direction of relative proper motion is much more likely for lens stars in the disk (assuming a bulge star source) than the $\sim -140^\circ$ angle that would be implied if star 2 were the lens star.

3.3. Interstellar Extinction

In order to apply the constraints from the high angular resolution follow-up images to the properties of the star plus planet lens system, we must account for the extinction in the foreground of the lens, and we also need the extinction to the source star in order to determine the angular source size. We determine the extinction in the foreground of the red clump giant stars following Bennett et al. (2014) using the red clump stars within $90''$ of the MOA-2008-BLG-379 event from the OGLE III photometry catalog (Szymański et al. 2011). We identify the peak of the red clump stars color–magnitude distribution to be at $I_{\text{rcg}} = 16.225 \pm 0.050$ and $(V - I)_{\text{rcg}} = 2.575 \pm 0.030$, as shown in Figure 3. Following Nataf et al. (2013), we take the extinction-corrected red clump giant magnitude and color to be $I_{\text{rcg}0} = 14.425$ and $(V - I)_{\text{rcg}0} = 1.06$. This gives extinction values of $A_I = 1.800$ and $A_V = 3.315$, implying a color excess of $E(V - I) = 1.515$. These values are within 0.5σ of the values quoted by Suzuki et al. (2014a, 2014b). We determine the K -band extinction, $A_K = 0.182$, from the Surot et al. (2020) value of the color excess at the location of MOA-2008-BLG-379, $E(J - K) = 0.369 \pm 0.0210$, using the Nishiyama et al. (2006) infrared extinction law, which gives $A_K/E(J - K) = 0.494 \pm 0.006$. We assume that the extinction for the source star is the same as the extinction of the center of the red clump giant distribution.

For the mass–luminosity relations, we must also consider the foreground extinction. At a Galactic latitude of $b = -3.1130^\circ$, and a lens distance of ~ 4 kpc, the lens system is likely to be behind most, but not all, of the dust that is in the foreground of the source. We assume a dust scale height of $h_{\text{dust}} = 0.10 \pm 0.02$ kpc (Drimmel & Spergel 2001), so that the extinction in the foreground of the lens is given by

$$A_{i,L} = \frac{1 - e^{-|D_L(\sin b)/h_{\text{dust}}|}}{1 - e^{-|D_S(\sin b)/h_{\text{dust}}|}} A_{i,S}, \quad (4)$$

where the index i refers to the passband: I , V , or K .

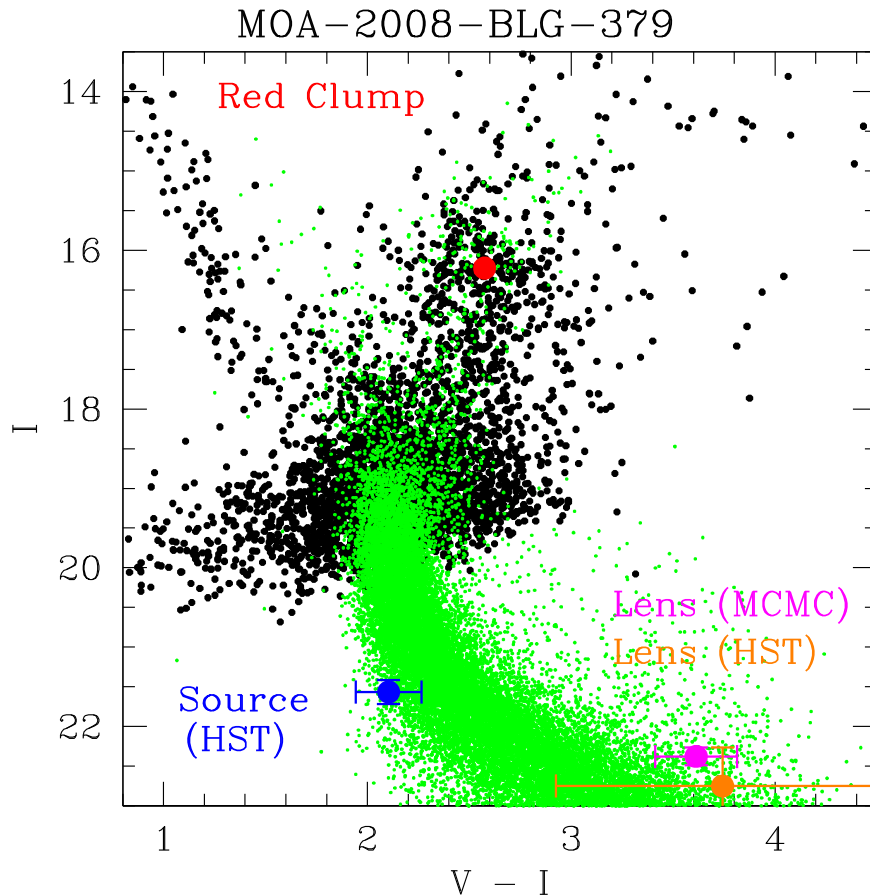


Figure 3. The color–magnitude diagram of OGLE III stars within 90 arcsec of microlensing event MOA-2008-BLG-379 (black dots), with the Hubble color–magnitude diagram of Baade’s window (green dots; Holtzman et al. 1998), transformed to the same extinction and Galactic bar distance as the MOA-2008-BLG-379 field. The red spot is the red clump giant centroid; the source and lens magnitudes from our Hubble observations are indicated in blue and orange. As Table 2 indicates, the V-band (F555W) Hubble images detect the lens star (star 1) at $\sim 1.2\sigma$ significance, so the Hubble measurements can be considered only an upper limit on the V-band brightness of the lens (and planetary host) star. The magenta spot indicates the lens star color and magnitude inferred from our Markov Chain Monte Carlo calculations using the constrained `eessunhong` light-curve modeling code. Since the lens star is likely to be in the disk or the near side of the bulge, it is typically brighter than the bulge main sequence.

4. Determination of Lens System Properties from Light-curve and High Angular Resolution Follow-up Data

For MOA-2008-BLG-379, like a number of other planetary events, we find it useful to apply constraints from the high angular resolution follow-up observations to the light-curve models. This can prevent the light-curve modeling from exploring parts of parameter space that are excluded by the high angular resolution follow-up observations. There are multiple ways to use light-curve modeling and high angular resolution follow-up observations to determine the masses and distance of a planetary microlensing system. But these methods can sometimes be compromised by astrophysical complications or systematic measurement errors. Thus, it is generally useful to confirm mass and distance measurements with multiple methods.

4.1. Light-curve Model and High Angular Resolution Image Parameters

This section discusses the parameters that are important for determining the physical properties of planetary microlensing systems from both light-curve modeling and high angular resolution imaging. The measurement of these parameters allows what is generally considered to be a “full solution” for a planetary microlensing system. The physical parameters that

result from these full solutions include the masses of the lens masses (both stars and planets) and their projected separation on the plane of the sky in physical units. On rare occasions, it is possible to determine more detailed properties of planetary microlensing systems, such as the orbital inclination and eccentricity (Gaudi et al. 2008; Bennett et al. 2010b), but this is much less likely for the cool low-mass planets that microlensing is uniquely sensitive to (Bennett & Rhie 1996, 2002). The parameters that are important for obtaining full solutions for planetary microlensing events are listed below, including parameters determined from both light-curve modeling and high angular resolution imaging.

1. Light-curve model parameters:
 - (a) The planet–star mass ratio, q . This is almost always measured with reasonable accuracy, but occasionally there are degeneracies, in which the light curve can be well fit by models with very different q values. Some of these degeneracies can be resolved with high angular resolution follow-up imaging (Terry et al. 2022).
 - (b) The Einstein radius crossing time, t_E . This is the time it takes for the lens–source relative motion to traverse the angular Einstein radius, θ_E . This is typically well measured, but there can be large uncertainties for faint

source stars with planetary signals observed at high magnification because t_E must be measured from the low-magnification part of the light curve (Di Stefano & Esin 1995; Alard 1997). The microlensing parallax signal, discussed below in item 1(e), also tends to be found in the lower-magnification parts of the light curve, so constraints on the microlensing parallax signal may also constrain t_E .

- (c) The source star magnitude and color, corrected for extinction, that is, I_{S0} and $(V_{S0} - I_{S0})$. This can be used to determine the source star's angular radius, θ_* (Kervella et al. 2004; Boyajian et al. 2014; Adams et al. 2018). When the blending degeneracy (Di Stefano & Esin 1995; Alard 1997) makes the t_E value very uncertain, the source magnitude also has a large uncertainty, so the inferred source star angular radius, θ_* , inherits a large uncertainty.
- (d) The source star radius crossing time, t_* . This is a measure of finite source effects in a microlensing light curve. More than half of the known planetary microlensing events allow t_* to be measured, and this allows the angular Einstein radius, $\theta_E = t_E \theta_*/t_*$, and the lens–source relative proper motion, $\mu_{\text{rel,G}} = \theta_*/t_*$, to be measured for most planetary events. Most microlensing modeling uses the instantaneously geocentric inertial reference frame that moves with the Earth's velocity at the time of the event peak. We use the subscript G to indicate that this geocentric frame has been used to measure the relative proper motion, $\mu_{\text{rel,G}}$.
- (e) The microlensing parallax, π_E . This is a two-dimensional vector caused by the fact that the microlensing event looks different to observers with different positions or velocities. This is most commonly observed due to the orbital motion of the Earth (Gould 1992; Alcock et al. 1995), but in some cases it can be measured by a satellite far from the Earth (Udalski et al. 2015) or from different observatories on the Earth (Gould et al. 2009). When the orbital motion of the Earth enables a π_E measurement for a microlensing event toward the Galactic bulge, the east component of π_E is usually measured much more accurately than the north component, because the orbital acceleration of the Earth perpendicular to the line of sight to the bulge is primarily in the east–west direction. This was the case for two previous planetary microlensing events with masses and distances determined with the help of high angular resolution follow-up observations (Bhattacharya et al. 2018; Bennett et al. 2020).

2. Parameters from high angular resolution imaging:

- (a) Excess flux at the location of the source star. This could be due to the lens star, but in some cases this can be due to a binary companion to the source or the lens or even an unrelated star (Bhattacharya et al. 2017). See Koshimoto et al. (2020) for a Bayesian method to address these issues.
- (b) Lens star magnitude(s). When the lens star has a measurable separation from the source star, it is possible to measure its brightness with a much lower probability of confusion with a star other than the lens. Magnitude measurements in multiple passbands can

provide a means for independent mass measurements that can be compared for consistency (Batista et al. 2015; Bennett et al. 2015).

- (c) Source star magnitudes or magnitude limits. While the source star magnitudes are usually determined by the microlensing light-curve modeling, the blending degeneracy can interfere with the source magnitude determination, as mentioned in item 1(c) above. In these cases, source magnitude measurements or limits from high-resolution imaging can be useful.
- (d) The lens–source relative proper motion in the heliocentric coordinate system, $\mu_{\text{rel,H}}$. This is determined from high angular resolution follow-up images when the lens–source separation can be measured. It can be used to help determine the microlensing parallax vector, π_E , because $\pi_E \parallel \mu_{\text{rel,G}}$, but this requires a change from the heliocentric to geocentric coordinate systems.

4.2. Microlensing Event Mass–distance Relations

Both the angular Einstein radius, θ_E , and the length of the microlensing parallax vector, π_E , give relations that link the lens system mass to the lens and source distances, D_S and D_L . These relations are (Bennett 2008; Gaudi 2012)

$$M_L = \frac{c^2}{4G} \theta_E^2 \frac{D_S D_L}{D_S - D_L}, \quad (5)$$

and

$$M_L = \frac{c^2}{4G} \frac{\text{AU}}{\pi_E^2} \frac{D_S - D_L}{D_S D_L}. \quad (6)$$

Equations (5) and (6) can be combined to yield the lens mass in an expression with no dependence on the lens or source distance,

$$M_L = \frac{c^2 \theta_E \text{AU}}{4G \pi_E} = \frac{\theta_E}{(8.1439 \text{ mas}) \pi_E} M_\odot. \quad (7)$$

The lens system distance can also be determined from

$$D_L = \frac{\text{AU}}{\pi_E \theta_E + 1/D_S}, \quad (8)$$

but it does depend on D_S . With clear measurements of both θ_E and π_E , it is possible to get a complete solution to a planetary microlensing event without the benefit of high angular resolution imaging, but this is relatively rare. Strong π_E measurements are generally obtained only for relatively long duration events with bright source stars that occur toward the beginning or end of the Galactic bulge observing season, when the orbital acceleration of the Earth is approximately perpendicular to the line of sight to the bulge (Muraki et al. 2011).

High angular resolution follow-up images can allow the source and lens stars to be resolved (Batista et al. 2015; Bennett et al. 2015; Vandorou et al. 2020) or partially resolved (Bhattacharya et al. 2018; Bennett et al. 2020) and enable their magnitudes to be measured. A measured magnitude of the lens star yields the following relation when the K -band brightness of the lens is measured:

$$K_L = 10 + 5 \log_{10}(D_L/1 \text{ kpc}) + \mathcal{M}_K(M_L) + A_{K,L}, \quad (9)$$

where $\mathcal{M}_K(M_L)$ is a K -band mass–luminosity relation. This requires the knowledge of the dust extinction, $A_{K,L}$, in the foreground of the lens star. In most cases, an empirical mass–luminosity relation for a main-sequence star is appropriate, but for host stars of $\sim 1 M_\odot$, the luminosity may change significantly over the age of the Galaxy, so a collection of isochrones is likely to be more accurate (Beaulieu et al. 2016; Vandorou et al. 2020). Mass–luminosity relations in multiple passbands can be used to confirm the mass measurement (Batista et al. 2015; Bennett et al. 2015), but they can also be used to identify circumbinary planets (Bennett et al. 2016), since the binary star systems have redder colors than single stars of the same mass (Terry et al. 2021).

These same high angular resolution follow-up images that resolve or partially resolve the lens and source stars can also be used to confirm the identification of the lens star by measuring the lens–source relative proper motion, $\boldsymbol{\mu}_{\text{rel}}$, which can be compared to the magnitude of the relative proper motion vector, $\mu_{\text{rel,G}} = \theta_*/t_*$, which can often be determined from the angular source star radius, θ_* , and source radius crossing time, t_* , from the light-curve model. However, these two independent $\boldsymbol{\mu}_{\text{rel}}$ values are not measured in the same reference frame. The light-curve model provides $\mu_{\text{rel,G}}$ in the instantaneously geocentric inertial reference frame that moves with the Earth at the time of peak magnification, while the high angular resolution follow-up imaging gives the two-dimensional vector proper motion, $\boldsymbol{\mu}_{\text{rel,H}}$, in the heliocentric reference frame (plus a small correction due to geometric parallax, which is usually negligible). The two-dimensional vector proper motions in the different reference frames are usually quite similar, but the difference can be significant if the relative proper motion or the lens distance, D_L , is small. The geocentric relative proper motion, $\boldsymbol{\mu}_{\text{rel,G}}$, can be determined with the following formula (Dong et al. 2009b):

$$\boldsymbol{\mu}_{\text{rel,G}} = \boldsymbol{\mu}_{\text{rel,H}} - \frac{\mathbf{v}_\oplus \pi_{\text{rel}}}{\text{AU}}, \quad (10)$$

where \mathbf{v}_\oplus is the projected velocity of the Earth relative to the Sun (perpendicular to the line of sight) at the time of peak magnification. The projected velocity for MOA-2008-BLG-379 is $\mathbf{v}_{\oplus, \text{N}} = (19.680, -2.5983) \text{ km s}^{-1} = (4.152, -0.548) \text{ au yr}^{-1}$ at the peak of the microlensing light curve, $\text{HJD}' = 4688$. The relative parallax is defined as $\pi_{\text{rel}} \equiv 1/D_L - 1/D_S$, where D_L and D_S are lens and source distances, so Equation (10) can be written as

$$\boldsymbol{\mu}_{\text{rel,G}} = \boldsymbol{\mu}_{\text{rel,H}} - (4.152, -0.548) \times (1/D_L - 1/D_S), \quad (11)$$

when D_L and D_S are given in units of kiloparsec and $\boldsymbol{\mu}_{\text{rel,H}}$ and $\boldsymbol{\mu}_{\text{rel,G}}$ are in units of milliarcseconds/year. Thus, a precise comparison of $\boldsymbol{\mu}_{\text{rel,H}}$ from high angular resolution follow-up observations to $\boldsymbol{\mu}_{\text{rel,G}}$ from the light-curve model requires some knowledge of D_L and D_S , but in many cases, a precise comparison may not be needed. For example, Bhattacharya et al. (2017) found that a candidate host star for the planet MOA-2008-BLG-310Lb was moving toward the source instead of away from it after the event. This showed that the likely host star suggested by Janczak et al. (2010) was actually not related to the microlensing event. This same argument was used to exclude a main-sequence candidate for the MOA-2010-BLG-477L host star (Blackman et al. 2021), leading to the

conclusion that this lens system is the first example of a planet in a wide orbit about a white dwarf host star.

The measurement of $\boldsymbol{\mu}_{\text{rel,H}}$ is also very useful for the determination of precise values for the microlensing parallax parameter, π_E . In most cases, one component of this two-dimensional vector is measured more precisely than the other. This is the component of π_E that is parallel to the orbital acceleration of the observer, and for microlensing events observed toward the Galactic bulge, the direction that is measured more precisely is quite close to the east–west direction, so it is usually the case that the east component of π_E is measured precisely, while the north component is only weakly constrained. Fortunately, the microlensing parallax vector, $\boldsymbol{\pi}_E$, is parallel to the $\boldsymbol{\mu}_{\text{rel,G}}$ vector, which can often be determined very precisely, using Equation (10), when we have a good measurement of $\boldsymbol{\mu}_{\text{rel,H}}$. The microlensing parallax and geocentric relative proper motion are related by

$$\boldsymbol{\pi}_E = \frac{\pi_{\text{rel}} \boldsymbol{\mu}_{\text{rel,G}}}{t_E |\boldsymbol{\mu}_{\text{rel,G}}|^2}, \quad (12)$$

so with measurements of $\pi_{E,E}$ and $\boldsymbol{\mu}_{\text{rel,H}}$, we can use Equations (10) and (12) to solve for $\pi_{E,N}$ (Gould et al. 1994; Ghosh et al. 2004; Bennett et al. 2007). This leads to a quadratic equation in order to solve for $\pi_{E,N}$ (Gould 2014), but in general, there is no ambiguity between the two solutions, as one solution either requires a negative lens distance, D_L , or predicts a lens brightness that is strongly inconsistent with the measured lens magnitude (Bhattacharya et al. 2018). This method was used to solve for $\pi_{E,N}$ to yield a precise measurement of the $\boldsymbol{\pi}_E$ vector for both OGLE-2005-BLG-071 (Bennett et al. 2020) and OGLE-2012-BLG-0950 (Bhattacharya et al. 2018), and in both cases, the microlensing parallax measurement confirmed the lens system masses and distance indicated by the host star brightness and θ_E values.

4.3. Applying Constraints from High Angular Resolution Follow-up Observation on Light-curve Models

In principle, one can determine the physical parameter of the host star plus planet lens system with independent analyses of the light curve and high angular resolution follow-up observations. This has been done for the planetary microlensing event OGLE-2005-BLG-169 (Batista et al. 2015; Bennett et al. 2015), but there are several potential problems with this approach. First, it can be the case that the follow-up data restrict the parameters of the lens system to a very small fraction of the parameter space volume that was consistent with the observed light curve. This then makes Markov Chain Monte Carlo (MCMC) calculations of the distribution of light-curve parameters very inefficient since most of the light-curve models accepted by the Markov chain are excluded by the follow-up observation constraints. This is particularly true for events that have partial measurements of the microlensing parallax effect, due to the orbital motion of the Earth (Bhattacharya et al. 2018; Bennett et al. 2020). Since the microlensing parallax vector points in the same direction as the lens–source relative proper motion vector, the follow-up observations exclude a large fraction of the models that are consistent with the light-curve data.

There are also a variety of both subtle microlensing features and systematic photometry errors that are easier to diagnose

with the help of the high angular resolution imaging data. Microlensing parallax is one such feature that is present in every light curve produced by a telescope in a heliocentric orbit, but the microlensing parallax signal is often too weak to be clearly detected. If the source star is in a binary system, then it can have orbital motion that also affects the light curve, similar to the microlensing parallax due to the orbital motion of the observer. This is known as xallarap. A binary companion to the source can also be microlensed, but this possibility is usually not considered, unless the companion has a dramatic influence on the light curve (Bennett et al. 2018) or if there is some danger of a binary source feature being interpreted as a planetary signal (Gaudi & Gould 1997; Beaulieu et al. 2006). The orbital motion of the planet can also have a significant effect on the light curve, but there is often some degeneracy between the orbital motion and the microlensing parallax (Gaudi et al. 2008; Bennett et al. 2010b) or xallarap parameters. Also, all three of these features (microlensing parallax, xallarap, the lensing of a binary companion to the main source star) can be mimicked by low-level systematic photometry errors.

Another problem can occur for high-magnification events with faint source stars, like the one analyzed in this paper, MOA-2008-BLG-379. High-magnification events are extremely sensitive to planetary signals (Griest & Safizadeh 1998; Rhie et al. 2000), and the faintness of the source star makes it easier to detect the lens stars, which are usually fainter than the source stars. However, it can be a challenge to determine the brightness of the source stars for such events, because of a degeneracy between Einstein radius crossing time (t_E) and source brightness of microlensing events (Di Stefano & Esin 1995; Alard 1997), which can only be resolved with relatively high precision photometry obtained at low magnification. Thus, the measurement of t_E and the source brightness is sensitive to low-level systematic photometry errors. Furthermore, the shape of the light curves at low magnification can also depend on microlensing parallax effects, so it is prudent to include microlensing parallax in the light-curve modeling, because the orbital motion of the Earth always produces a microlensing parallax signal that could affect the light-curve constraints on t_E and the source brightness.

In order to address this problem, we have modified our fitting code (Bennett & Rhie 1996; Bennett 2010), which now goes by the name, `eesunhong`,¹² in honor of the original coauthor of the code (Bennett 2014; Bennett & Khavinson 2014). This new version of `eesunhong` includes the constraints on the brightness and separation of the lens and source stars from the high angular resolution follow-up images from Keck AO and Hubble. However, in order to determine the mass of the host star based on the lens–source relative proper motion, which determines the angular Einstein radius, θ_E , we need to know the distance to the source star, D_S , so that we can use the mass–distance relation given in Equation (5). This requires us to include the source distance, D_S , as a light-curve model parameter, and we include a weighting from the Koshimoto et al. (2021a) Galactic model as a prior for the D_S parameter. We also use the Koshimoto et al. (2021a) Galactic model to provide a prior for the distance to the lens for a given value of the D_S parameter. However, this prior for D_S at fixed D_L is used to weight the entries in a sum of Markov chain values, rather than directly in the light-curve modeling code.

The light-curve modeling code does use constraints from the Keck analysis for $\mu_{\text{rel,H}}$ that are given in Table 1 and on the lens magnitude, $K_L = 18.815 \pm 0.106$, based on our identification from the Hubble analysis that star 1 is the lens (and planetary host) star. The K_L error bar is larger than the value of 0.056 quoted for the K_L measurement in Section 3.1 because we have added a K -band mass–luminosity relation uncertainty of 0.09 mag in quadrature to the measurement uncertainty. This constraint is implemented with a Gaussian distribution χ^2 contribution to the total model χ^2 . The measured Hubble source and lens magnitudes are $I_S = 21.557 \pm 0.149$ and $I_L = 22.742 \pm 0.488 \pm 0.190$, where the ± 0.190 uncertainty is our estimate of the I -band mass–luminosity relation uncertainty. This implies $I_L = 22.742 \pm 0.524$. We also apply a constraint to the combined brightness of the lens and source, as this is measured more precisely than the individual lens and source magnitudes. Our Hubble measurement finds $I_{S+L} = 21.243 \pm 0.011$, but we add a systematic uncertainty of 0.10 mag to this value to account for the mass–luminosity relation uncertainty for the lens star and any systematic error that might be caused by measurement of the combined brightness of two partially resolved stars. This yields our constraint value of $I_{S+L} = 21.243 \pm 0.101$. The light curve does not provide a good measurement of the source V -band magnitude, so we do not attempt to constrain that, but the Hubble data do provide an upper limit on the V -band brightness of the lens star, which is a lower limit on the magnitude: $V_L \geq 26.493 \pm 0.684$. This limit implies a Gaussian contribution to χ^2 for models with $V_L < 26.493$ with no χ^2 contribution for models with $V_L \geq 26.493$.

Table 3 shows the parameters of our four degenerate light-curve models and the Markov chain average of all four models. The parameters that apply to single-lens models are the Einstein radius crossing time, t_E , the time of closest alignment between the source and the lens system center of mass, t_0 , and the distance of closest approach between the source and the lens system center of mass, u_0 , which is given in units of the Einstein radius. The addition of a second lens mass requires three additional parameters, the mass ratio of the two lens masses, q , their separation, s , in units of the Einstein radius, and angle, α , between the source trajectory and the transverse line that passes through the two lens masses. In addition, a large fraction of binary lens systems exhibits finite source effects that can be modeled with the addition of the source radius crossing time parameter, t_* . We include the north and east components of the microlensing parallax vector $\pi_{E,N}$ and $\pi_{E,E}$ that are defined in an inertial “geocentric” coordinate system that is fixed to the Earth’s orbital velocity at $t_{\text{fix}} = 4688$. For each passband (MOA-red, OGLE I, and OGLE V) there are two linear parameters to describe the source flux and the blend flux (which accounts for blended starlight that is not absorbed in the \sim uniform sky background). Following Rhie et al. (1999), the source and blend fluxes are determined by a linear fit to the model with all the other parameters fixed. These constrained models have 3617 observations, 10 nonlinear parameters, six linear parameters, and eight constraints for a total of 3609 degrees of freedom.

For high-magnification events, like MOA-2008-BLG-379, the transformation $s \rightarrow 1/s$ often has only a slight change on the shape of the light curve. This is often referred to as close-wide degeneracy (Dominik 1999), and it applies to MOA-2008-BLG-379. However, as with many other events, the

¹² <https://github.com/golmschenk/eesunhong>

Table 3
Best-fit Model Parameters with $\mu_{\text{rel,H}}$ and Magnitude Constraints

Parameter	$u_0 < 0$		$u_0 > 0$		MCMC Averages
	$s < 1$	$s > 1$	$s < 1$	$s > 1$	
t_E (days)	55.637	55.087	55.452	55.527	55.8 ± 5.5
t_0 (HJD')	4687.8953	4687.8742	4687.8952	4687.8739	4687.8795 ± 0.0091
u_0	-0.0047088	-0.0055301	0.0047275	0.0055000	-0.00529 ± 0.00054
s	0.92651	1.08670	0.92706	$(u_0 > 0)$	0.929 ± 0.007
				$(s > 1)$	
α (rad)	-1.13442	-1.13131	1.13417	1.13111	-1.1320 ± 0.0023
$q \times 10^3$	5.2320	5.3139	5.2398	$(u_0 > 0)$	5.37 ± 0.41
				$(s > 1)$	
t_* (days)	0.02191	0.02216	0.02183	0.02219	0.0221 ± 0.0008
$\pi_{\text{E,N}}(t_{\text{fix}} = 4688)$	0.07313	0.07442	0.07518	0.07541	0.080 ± 0.026
$\pi_{\text{E,E}}(t_{\text{fix}} = 4688)$	0.19663	0.19697	0.19594	0.19540	0.207 ± 0.037
D_s (kpc)	8.2542	8.0907	8.2568	8.3499	8.11 ± 1.32
fit χ^2	1291.94	1290.01	1292.24	1290.07	...
dof	~ 1276	~ 1276	~ 1276	~ 1276	...

Table 4
Measurement of Planetary System Parameters from the Lens Flux Constraints

Parameter	Units	Values and rms	2σ Range
Angular Einstein Radius, θ_E	mas	0.754 ± 0.040	0.672–0.832
Geocentric lens-source relative proper motion, $\mu_{\text{rel,G}}$	mas yr ⁻¹	5.042 ± 0.149	4.70–5.29
Host star mass, M_{host}	M_\odot	0.434 ± 0.065	0.307–0.561
Planet mass, m_p	M_{Jup}	2.44 ± 0.49	1.56–3.47
Host star—Planet 2D separation, a_\perp	au	2.70 ± 0.42	1.87–3.53
Host star—Planet 3D separation, a_{3D}	au	$3.3^{+1.8}_{-0.6}$	2.1–12.9
Lens distance, D_L	kpc	3.44 ± 0.53	2.44–4.53
Source distance, D_S	kpc	7.77 ± 1.27	5.19–10.24

MOA-2008-BLG-379 does not strictly meet the close-wide degeneracy conditions that make the central caustic nearly identical under the $s \leftrightarrow 1/s$ transformations. Of course, a microlensing light curve only samples a fraction of the microlensing magnification pattern, so this is not really a surprise. Zhang et al. (2022) have examined this situation systematically and have explained in more detail the conditions needed for this degeneracy, which they refer to as the offset degeneracy (although the term “central caustic offset degeneracy” would be more descriptive).

This event, like most Galactic bulge microlensing events, is also subject to the ecliptic degeneracy (Poindexter et al. 2005), which is exact for events in the ecliptic plane. This degeneracy involves replacing a binary lens system with its mirror image, and it is the orbital motion of the Earth, which is detected via the microlensing parallax effect, that breaks the mirror symmetry. The models with the different lens system orientations have opposite signs for the u_0 and α parameters. The light-curve data for MOA-2008-BLG-379 do not provide a strong signal for the microlensing parallax effect, and we have only included microlensing parallax in our modeling because the high angular resolution imaging constrains the microlensing parallax parameters and these parameters might be correlated with other model parameters. The best-fit models that differ by this ecliptic degeneracy (with $u_0 < 0$ and $u_0 > 0$) are nearly identical, but the best-fit wide model with a planet–star projected separation of $s = 1.08132$ is a slightly better fit than the best-fit close model with $s = 0.93472$ by $\Delta\chi^2 = 1.93$.

In order to check the consistency of the high angular resolution observation constraints with the light-curve data, we

can compare the χ^2 values for the best-fit models with and without these constraints. The best-fit constrained model has $\chi^2 = 1290.01$ for 1287 light-curve photometry measurements, while the best unconstrained model has $\chi^2 = 1285.27$, for a difference of $\Delta\chi^2 = 4.74$. A total of eight constraints were imposed on the light-curve models. These were constraints on two components of $\mu_{\text{rel,H}}$, three constraints on the lens star magnitudes (K_L , I_L , and V_L), one constraint of the source star magnitude, I_S , one constraint on the combined source plus lens star magnitude, I_{S+L} , and one constraint on the source star distance, D_S . This $\Delta\chi^2 = 4.74$ increase had contributions of 1.59 from the light-curve fit, 0.41 from the $\mu_{\text{rel,H}}$ constraint, 1.87 from the three lens magnitude constraints, 0.08 from the I_S constraint, 0.70 from the I_{S+L} constraint, and 0.10 from the source distance constraint. Thus, there appears to be no conflict between the light-curve data used in the analysis and the constraints from the high angular resolution follow-up observations.

5. Lens Properties

Table 4 and Figure 4 provide the results of our analysis. These results were obtained by summing over the MCMC results that are summarized in Table 3 to determine the posterior distribution of the properties of the MOA-2008-BLG-379L planetary system. We have run four Markov chains for each of the χ^2 minima listed in Table 3, and we have applied a weight of $e^{-\Delta\chi^2/2}$ to the Markov chains, with $\Delta\chi^2$ defined as the difference between the best-fit χ^2 for each χ^2 minima compared to the overall best-fit χ^2 , which was the $u_0 < 0$, $s > 1$

MOA–2008–BLG–379 Properties with Keck & HST Constraints

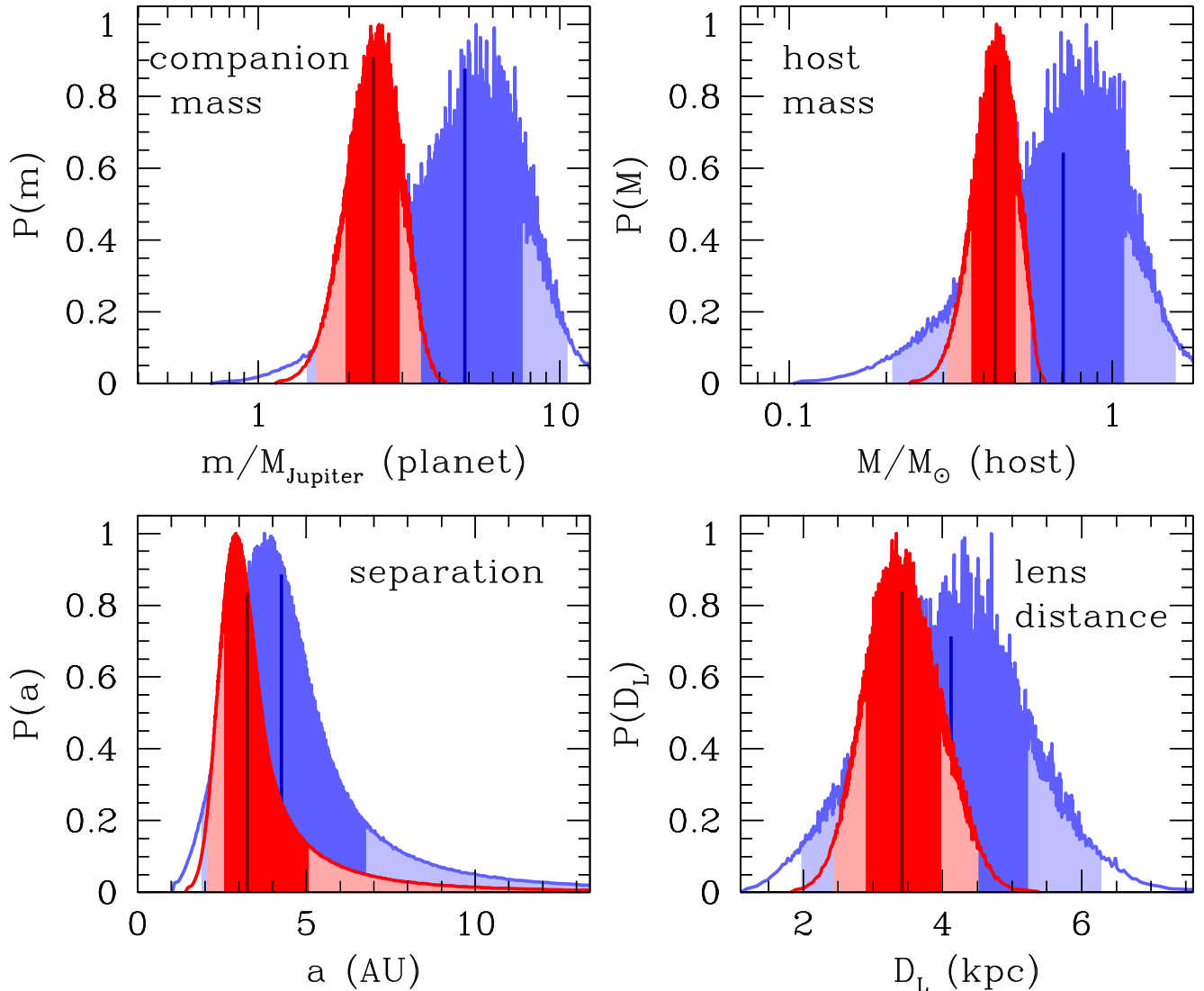


Figure 4. The Bayesian posterior probability distributions for the planetary companion mass, host mass, their separation, and the distance to the lens system are shown with only light-curve constraints in blue and with the additional constraints from our Keck and Hubble follow-up observations in red. The central 68.3% of the distributions are shaded in darker colors (dark red and dark blue), and the remaining central 95.4% of the distributions are shaded in lighter colors. The vertical black line marks the median of the probability distribution of the respective parameters.

model. With the burn-in phases of the Markov chains removed, there were a total of 105,0161 accepted Markov chain steps used in these calculations.

Because we constrained lens–source relative proper motion, $\mu_{\text{rel,H}}$, the host star K , I , and V magnitudes, and the combined host and source star magnitudes in the light-curve modeling, we do not apply these constraints when summing the MCMC results. Also, since the source distance, D_S , prior was applied to the light-curve model, we do not apply it again. However, we do use a Galactic model prior on the lens distance, D_L , for the D_S value for each light-curve model, constrained by the measured $\mu_{\text{rel,H}}$ value.

Thus far, we have assumed that all stars are equally likely to host the planet with the measured mass ratio q . This is a common assumption, but we do not have any empirical evidence that it is true. In fact, as mentioned in the introduction, the preliminary evidence from both microlensing and radial velocity surveys indicates that the planet hosting probability

scales in proportion to the host star mass. Therefore, we have applied a prior proportional to M_{host} to our sum over the MCMC results. Fortunately, because the light-curve and high-resolution imaging data constrain the mass, this prior has a small effect on the results. The results presented in Table 4 and Figure 4 change by $<0.2\sigma$ if we switch to the more common (but likely incorrect) prior assumption that the planet hosting probability is independent of host mass.

We find that the host star has a mass of $M_{\text{host}} = 0.434 \pm 0.065 M_{\odot}$ and that it is orbited by a super-Jupiter mass planet with $m_p = 2.44 \pm 0.49 M_{\text{Jup}}$ at a projected separation of $a_{\perp} = 2.70 \pm 0.42$ au. This translates to a three-dimensional separation of $a_{3d} = 3.3^{+1.8}_{-0.6}$ au under the assumption of a random orientation of the planetary orbit, and the lens system is located at a distance of $D_L = 3.44 \pm 0.53$ kpc. These distributions are indicated by the red histograms in Figure 4. These results are a dramatic improvement in precision over the

blue histograms, which indicate the parameters predicted by our Bayesian analysis without any constraints from Keck or Hubble observations.

While high angular resolution follow-up observations provide much more precise determinations of the properties of the planetary system responsible for the microlensing event, there is one significant inconsistency between the analysis with and without the high angular resolution follow-up observations. We have found the Einstein radius crossing time to be $t_E = 55.8 \pm 5.5$ days, which is noticeably larger than the value of $t_E = 45.0 \pm 6.2$ days obtained in our analysis without the high angular resolution follow-up observation constraints and the discovery paper (Suzuki et al. 2014a, 2014b) value of $t_E = 42.3 \pm 0.5$ days. The longer t_E value is due to the fact that the Hubble and Keck data imply a source that is 0.32 mag fainter than the value from the discovery paper. The discovery paper used the unphysical constraint $\pi_E \equiv 0$, which could, in some cases, lead to unphysically small error bars on t_E (e.g., Sumi et al. 2010; Batista et al. 2011), but in this case, the small error bars were reported because the MCMC analysis was not run long enough to have converged. This constraint does not come directly from the Hubble I_S measurement due to the large correlated uncertainty in the fractions of I -band flux attributed to the source and lens stars. This is due to their relatively small separation at the time of the Hubble observations. The fainter source star is implied by the combination of constraints from all three passbands including the tight constraint on the combined I -band brightness of the lens and source stars, as well as the lens–source relative proper motion, $\mu_{\text{rel,H}}$, constraint. If the lens–source separation had been larger at the time of the Hubble images, the direct I_S measurement would be more precise. In this case, it would provide a precise constraint on t_E .

Despite the inconsistency between our models and the Einstein radius crossing time, t_E , and the source brightness values from Suzuki et al. (2014a, 2014b), our results for the lens system masses and distance fall within the ranges $M_{\text{host}} = 0.56^{+0.24}_{-0.27} M_{\odot}$, $m_p = 4.1^{+1.7}_{-1.9} M_{\text{Jup}}$, and $D_L = 3.3^{+1.3}_{-1.2}$ kpc quoted in that paper. This is partly because the uncertainties in these parameters are large without the follow-up observations but also because the larger t_E partially compensates for the smaller angular source star radius, θ_* , in the calculation of the angular Einstein radius, $\theta_E = t_E \theta_* / t_*$.

6. Lessons for Modeling Roman Galactic Exoplanet Survey Events

The original version of this paper attributed a $\sim 30\sigma$ difference between the Einstein radius crossing time predicted by the MOA-2008-BLG-379Lb discovery paper Suzuki et al. (2014a, 2014b) to the fact that the models in this paper fixed the microlensing parallax parameter to $\pi_E \equiv 0$. This is a common procedure, but it could lead to unphysical constraints on the other light-curve parameters. However, as we explain in the Appendix, this is not the case for the MOA-2008-BLG-379 event. However, this is the case for three other events (out of 28) in the Suzuki et al. (2016) statistical sample. The t_E values for microlensing parallax models differ from the values with $\pi_E \equiv 0$ by 17σ , 12σ , and 6.3σ for OGLE-2007-BLG-368 (Sumi et al. 2010), MOA-2009-BLG-387 (Batista et al. 2011), and OGLE-2012-BLG-0563 (Fukui et al. 2015), respectively. This difficulty in determining t_E and the source star magnitude for high-magnification events with faint sources is a general one, due to the fact that it is the low-magnification regions of a

single-lens light curve that provide the strongest constraints on t_E and the source brightness (Yee et al. 2012). This may play a role in the failure of the $\pi_E \equiv 0$ modeling to produce a reasonable t_E error bar for OGLE-2012-BLG-0563, but there is likely to be a different source of the t_E error bar problems for OGLE-2007-BLG-368 and MOA-2009-BLG-387, since these events have more modest magnification. Both of these events have strong, caustic crossing features that strongly break the circular symmetry of a single-lens magnification pattern. This makes these events much more sensitive to microlensing parallax effects.

The analysis of the MOA-2008-BLG-379 high-resolution imaging data has illustrated some ways in which light-curve modeling can be improved when one is trying to determine the physical parameters of the lens system with the help of high angular resolution imaging to measure the brightness and separations of the lens stars from the microlensing source stars. The high angular resolution images obtained for the exoplanet microlensing survey of the Roman Space Telescope (Bennett et al. 2018a; Penny et al. 2019; Johnson et al. 2020) have long been thought to play a key role in the measurement of host star and planet masses for the planetary systems discovered in Roman’s Galactic Bulge Time Domain Survey (Bennett & Rhie 2002; Bennett et al. 2007). Our Keck and Hubble observations of the microlens planetary systems from the Suzuki et al. (2016) statistical sample have found that the previous analyses of most of these planetary microlensing events had to be redone in order to determine the masses and distance of these lens systems.

The inclusion of constraints from the high angular resolution imaging in the light-curve modeling has proved to be very useful. For our analysis of MOA-2008-BLG-379, modeling with these constraints has helped to recognize the importance of including microlensing parallax in the modeling even when there is little or no evidence of a measurable microlensing parallax signal in the data. This is because constraining $\pi_E = 0$ can impose incorrect constraints on t_E and the source brightness. However, it can also be necessary to avoid unphysically large π_E values by applying a prior based on a Galactic model. Similar constraints have made the modeling of events with accurate measurements of only one component of the two-dimensional π_E vector much more efficient by excluding a very large fraction of models that are consistent with the light curve but not consistent with the direction of lens–source relative proper motion, $\mu_{\text{rel,H}}$, measured from the high angular resolution follow-up data (Bhattacharya et al. 2018; Bennett et al. 2020).

Since the very first discovery of a microlensing event, it has been quite common for modelers to ignore the effects of “higher-order effects” when they do not seem necessary to explain the data. These higher-order effects include microlensing parallax, planetary orbital motion, additional lens mass, and a binary companion to the source, which may also be microlensed or can generate detectable orbital motion for the source star, which is known as “xallarap.” This procedure, favoring the minimal model that can explain the data, is considered preferable when establishing the detection of some new light-curve feature, such as the first microlensing parallax detection (Alcock et al. 1995) or the first exoplanet found by microlensing (Bond et al. 2004). In fact, the binary lens nature of the very first microlensing event detected (Dominik & Hirshfeld 1994; Rhie & Bennett 1996) was ignored in the

discovery paper (Alcock et al. 1993). In the case of MOA-2008-BLG-379, the apparent systematic photometry errors leading to unphysically large π_E values provided an additional motivation to exclude microlensing parallax from the light-curve models.

However, we know that every planetary microlensing event has both microlensing parallax and planetary orbital motion. All telescopes are on orbits about the Sun, and bound planets orbit their host stars, so these effects will always be present. Even if the data do not have sufficient precision to measure these effects, they can still influence the uncertainties on other parameters of interest, such as the source star brightness and Einstein radius crossing time (t_E), as we have seen for this event. The situation is somewhat similar for planetary event MOA-2007-BLG-192, which involved a source star only slightly brighter than the MOA-2008-BLG-379 source. This event was published with a large π_E value (Bennett et al. 2008) that turned out to be contaminated by a systematic error (Koshimoto et al. 2021b; Terry et al. 2024) due to the color dependence of atmospheric refraction (Bennett et al. 2012). This error would likely have been found earlier if a prior distribution for π_E had been used in the modeling.

The orbital motion of the planet can often produce effects similar to microlensing parallax (Bennett et al. 2010b; Sumi et al. 2016), so most of the planets in the Suzuki et al. (2016) sample with microlensing parallax measurements also have had planetary orbital motion included in their models (Gaudi et al. 2008; Dong et al. 2009b; Batista et al. 2011; Muraki et al. 2011; Bachelet et al. 2012; Furusawa et al. 2013; Skowron et al. 2015; Bennett et al. 2016, 2018b). Thus, the orbital motion of the planetary (and possible stellar companions) to the host star should generally be included in the modeling to ensure an unbiased π_E measurement.

Another astrophysical effect that can interfere with π_E measurements is a binary companion to the source, which can induce source star orbital motion in a similar manner to the way that the Earth’s orbital motion can reveal the microlensing parallax effect. However, this is orbital motion at the location of the source rather than the observer. As a result, this source orbital motion, which is referred to as xallarap, is much stronger for lens systems close to the source, while microlensing parallax signals are stronger when the lens system is close to the observer. If the xallarap signal is similar to or larger than the parallax signal, it can generally be distinguished from parallax because light-curve models including the xallarap effect will have significantly improved χ^2 values compared with parallax models. This was the case for OGLE-2007-BLG-368 (Sumi et al. 2010). It is also possible for source companions to influence the photometric signal if the companion is not much fainter than the source star. For some events, such as MOA-2010-BLG-117 (Bennett et al. 2018b), the effect of the second lensed source is so dramatic that there is no single-source binary lens model that can provide even an approximate fit to the photometry data. However, it is also possible for a modest magnification of a companion to the source to slightly perturb the light curve away from the peak in such a way as to perturb the microlensing parallax signal. This was the case for event MOA-2010-BLG-328, which was published with two competing models (Furusawa et al. 2013), one with parallax and lens orbital motion and one with xallarap. However, the high angular resolution follow-up data from Keck and Hubble were not consistent with either of these

models. The Keck data identified the lens at the expected separation from the source, but there was additional stellar flux at the location of the source due to another star. A model including microlensing parallax, lens star plus planet orbital motion, and the orbital motion and microlensing magnification of the binary source system was able to match the positions and magnitudes of the lens and source stars from the Keck and Hubble images, as well as the light-curve data (Vandorou et al. 2024, in preparation).

In general, the modeling of planetary microlensing events is much simpler when the constraints from the high angular resolution imaging are included in the modeling, as discussed in Section 4.3. For events with one-dimensional π_E measurements, but no other higher-order effects, this constrained modeling primarily acts to improve the efficiency of MCMC calculations by excluding models that are inconsistent with the high angular resolution observations from the Markov chains. However, for events like MOA-2010-BLG-328, with measurable orbital motion and/or a source star companion, it becomes more likely that the modeling code will be unable to find the correct solution if constraints from the high angular resolution images are not imposed. The likelihood of modeling failures is increased if the parameters describing the higher-order effects are not constrained to physically reasonable values with a prior distribution.

Another benefit of using the high angular imaging constraints, as discussed in Section 4.3, is that the constraints can provide redundant measurements of the lens system mass and distance. These redundant measurements can then be used to help identify systematic errors in the photometry. This was the case for event OGLE-2012-BLG-0563 (Fukui et al. 2015), where systematic errors in some of the data from microlensing follow-up surveys were found to predict a source radius crossing time, t_* , that was not consistent with the lens–source separation as measured by both Keck AO and Hubble imaging (A. Bhattacharya et al. 2024, in preparation; D. P. Bennett et al. 2024, in preparation).

This problem with excluding higher-order effects when they do not appear to be necessary to explain the light curve was foreshadowed in Section 6.2 of Penny et al. (2016), which notes that six published planets had published distances of <2 kpc, when the Penny et al. (2016) simulations suggested that there should be only one such planetary microlensing event with the size of the sample they considered. One of these six events turned out not to have a planetary signal at all (Han et al. 2016), and one had a strong baseline photometry trend that was attributed to the proper motion of a nearby star. However, this was contradicted by more recent data (Udalski, private communication) suggesting that the large microlensing parallax value, $\pi_E \gtrsim 0.8$, for this event could be spurious. The remaining four events were part of our program of high angular resolution follow-up imaging for the 22 planetary microlensing events from the Suzuki et al. (2016) sample. Our analysis indicates that the previously claimed short lens distances for three of these events, MOA-2007-BLG-192 (Bennett et al. 2008; Terry et al. 2024), MOA-2010-BLG-328 (Furusawa et al. 2013), and OGLE-2012-BLG-0563 (Fukui et al. 2015), were wrong.

Like the event analyzed in this paper (MOA-2008-BLG-379), MOA-2007-BLG-192 is a high-magnification event with a source magnitude of $I_S \sim 21.5$, but it had a large π_E value that turned out to be due to a systematic error (Koshimoto et al.

2021b) caused by the color dependence of atmospheric refraction (Bennett et al. 2012). This error could have been detected if a Galactic π_E prior had been used, as this would have revealed that the extremely large π_E reported by Bennett et al. (2008) was highly improbable.

For a robust statistical analysis of a statistical sample of exoplanets found by microlensing, we argue that it is crucial to include all the higher-order microlensing events that can plausibly influence the results, even if the higher-order effects are not well constrained by the data. Otherwise, the values and uncertainties of other microlensing light-curve parameters can be influenced by physically incorrect constraints brought on by setting higher-order effect parameters to zero. It may be necessary to impose prior distributions on some of these higher-order effect parameters, such as microlensing parallax and lens orbital motion, to avoid biasing the results with highly unlikely values that may be consistent with the data. Note that these prior distributions should be based on actual Galactic data. (Many Bayesian analyses of planetary microlensing events assume that every possible host star has an equal probability to host a planet, with the measured mass ratio, q , but it is often not recognized that this is a prior assumption that is not based on any data.) It is also prudent to avoid priors that might be overly prescriptive, as these could interfere with somewhat unexpected discoveries. Section 6.2 of Penny et al. (2016) used a prior assuming that stars in the Galactic bulge were as likely to host planets and stars in the Galactic disk. This could certainly be considered to be overly prescriptive. However, the conclusion reached based on this prior provided by this prior was correct. The simulations of Penny et al. (2016) indicated that only one of the planetary systems in their sample should be located at a distance of ≤ 2 kpc, but papers published for six of the microlensing planetary systems in this sample indicated that six of these systems were located at distances of ≤ 2 kpc. Since then, the distance estimates of four of the claimed six planetary systems at $D_L \leq 2$ kpc have been shown to be wrong, while the distance estimate of one of these systems is now ambiguous due to a possible systematic photometry error. We also argue that it is best to impose the constraints from high angular resolution imaging to the light-curve modeling code. This can greatly speed up the analysis by avoiding the exploration of parts of the parameter space that are inconsistent with the high angular resolution imaging data. For some of the most complicated events, these constraints may be necessary to find the correct solutions. However, the possibility that an overly prescriptive prior might be interfering with the detection of a previously unknown property of planetary systems must also be considered.

The strengths of this approach are events from our group’s lens system mass and distance analysis of the 28 events (with 29 planets) in the Suzuki et al. (2016) statistical sample. (The “ambiguous event,” OGLE-2011-BLG-0950, from this sample was found to be due to a stellar binary lens system instead of a planetary system (Terry et al. 2022).) Six of these 28 events had giant source stars, which imply that detecting the exoplanet host star is virtually impossible with Hubble or Keck (although it may be possible with JWST), but two of these events (Muraki et al. 2011; Skowron et al. 2015) have mass measurements from π_E and θ_E measurements. This is also the case for one event, MOA-2010-BLG-117, which has a source system consisting of a binary pair of subgiants (Bennett et al. 2018b). We have obtained high angular resolution follow-up

imaging with Keck AO or Hubble for all 21 events without giant or binary subgiant source stars, and we have detected or determined the nature of the lens (and planetary host) star for 12 of them (Gaudi et al. 2008; Bennett et al. 2010b, 2015, 2016, 2020; Batista et al. 2015; Bhattacharya et al. 2018, 2021; Blackman et al. 2021; Terry et al. 2021, 2024), although the publications describing two of these events are still in preparation.

We have found that image-constrained modeling was necessary or useful for seven of the 12 events with detected host stars, and for at least three of these events (MOA-2008-BLG-379, MOA-2010-BLG-328, and OGLE-2012-BLG-0563), image-constrained modeling was instrumental in obtaining the correct solutions. The modeling of higher-order effects was also crucial for the mass and distance measurements. The three events with giant or binary subgiant source stars and masses from π_E measurements (MOA-2009-BLG-266, MOA-2010-BLG-117, and OGLE-2011-BLG-0265) included planetary orbital motion in their modeling. Higher-order effects, such as additional lens objects, an additional source, or lens orbital motion, were needed for the discovery papers for four of the 12 events with detected or characterized host stars (OGLE-2006-BLG-109, OGLE-2007-BLG-349, MOA-2010-BLG-117, and MOA-2010-BLG-477). Orbital motion of the lens or source system was also needed for two of the events without detected host stars, OGLE-2007-BLG-368 (Sumi et al. 2010) and MOA-2009-BLG-387 (Batista et al. 2011). However, higher-order effects beyond those presented in the discovery papers were needed to find the correct solutions for three of the 12 events with planetary host star detections, MOA-2008-BLG-379 (this paper), MOA-2009-BLG-319 (Shin et al. 2015; Terry et al. 2021), and MOA-2010-BLG-328 (Vandorou et al. 2024, in preparation).

We have argued that it is necessary to include higher-order effects in microlensing event modeling, even in cases where microlensing light curves can be fit reasonably well without including these effects. This is because these effects are certain, or reasonably likely to be present, and ignoring them can lead to errors in the values for the other microlensing light-curve parameters. This might not be considered to be a serious problem if the analysis goal is simply to indicate that the microlensing event is due to the planetary system, but it becomes more problematic in a statistical analysis of exoplanetary system properties from microlensing surveys, such as the one planned for the Roman Space Telescope (Bennett et al. 2018a; Penny et al. 2019; Johnson et al. 2020). A major advantage of Roman’s microlensing survey is its ability to detect the exoplanet host stars and determine the masses and distances of these systems using the methods that we have used for our Keck AO and Hubble follow-up analysis of planetary microlensing events observed from the ground. Therefore, we believe that image-constrained modeling will be needed to analyze the planetary microlensing events found by Roman.

7. Discussion and Conclusions

Our Keck AO and Hubble follow-up observations have identified the MOA-2008-BLG-379L planetary host star through measurements of the host star K -band magnitude, the source V -band magnitude, the lens and source I -band magnitudes, and the lens–source relative proper motion, $\mu_{\text{rel},H}$. These measurements constrained some of the light-

curve parameters and allowed us to determine host and planet masses and distance through multiple, redundant constraints. We find host and planet masses of $M_{\text{host}} = 0.434 \pm 0.065 M_{\odot}$ and $m_p = 2.44 \pm 0.49 M_{\text{Jup}}$, with a projected separation of $a_{\perp} = 2.70 \pm 0.42$ au at a distance of $D_L = 3.44 \pm 0.53$ kpc. These measurements imply that MOA-2008-BLG-379Lb is the third super-Jupiter mass planet, with a mass in the range $2\text{--}3.6 M_{\text{Jup}}$ orbiting a star of $\sim 0.43 M_{\odot}$ after OGLE-2005-BLG-071Lb (Dong et al. 2009b; Bennett et al. 2020) and OGLE-2012-BLG-0406 (Poleski et al. 2014; Tsapras et al. 2014). These discoveries may seem to disfavor the Laughlin et al. (2004) argument that gas giants should be rare orbiting M dwarfs, but such a judgment requires a more detailed statistical analysis. The analysis presented here is part of our campaign to measure masses for as many of the planets and host stars of the 29-planet complete sample of Suzuki et al. (2016) as possible. (Keck observations by Terry et al. (2022) of the ambiguous event from this sample favor the stellar binary model over the planetary model.) We have obtained Keck AO observations for all the events in this sample that have source stars with an extinction-corrected source magnitude of $I_{s0} > 16$ under a NASA Keck Key Strategic Mission Support program (Bennett 2019), and several of the brighter stars have host and planet mass measurements from a combination of microlensing parallax measurements and angular Einstein radius determinations from finite source effects (Gaudi et al. 2008; Bennett et al. 2010b, 2018b; Muraki et al. 2011; Skowron et al. 2015). Thus, we expect to be able to address this problem more definitively in a future paper that includes these mass measurements in a statistical analysis. However, a preliminary statistical analysis including some of these mass measurements does suggest that the planets found by microlensing, at the measured mass ratios, are more likely to be hosted by more massive stars. So, perhaps the Laughlin et al. (2004) argument does not preclude the hosting of super-Jupiter planets by M dwarfs because there is a large dispersion in the properties of protoplanetary disks, so even though the formation of super-Jupiters may be disfavored around M dwarfs, there are still a significant number of M dwarfs that can produce super-Jupiter planets despite this handicap.

Acknowledgments

The Keck Telescope observations and analysis were supported by a NASA Keck PI Data Award, administered by the NASA Exoplanet Science Institute. Data presented herein were obtained at the W. M. Keck Observatory from telescope time allocated to the National Aeronautics and Space Administration through the agency’s scientific partnership with the California Institute of Technology and the University of California. The observatory was made possible by the generous financial support of the W. M. Keck Foundation. D.P.B., A.B., N.K., S.K.T., and A.V. were also supported by NASA through grants 80NSSC20K0886 and 80GSFC21M0002. Some of this research has made use of the NASA Exoplanet Archive, which is operated by the California Institute of Technology, under contract with the National Aeronautics and Space Administration under the Exoplanet Exploration Program. This work was supported by the University of Tasmania through the UTAS Foundation and the endowed Warren Chair in Astronomy and the ANR COLD-WORLDS (ANR-18-CE31-0002). This work was also supported by JSPS Core-to-Core Program

JPJSCCA20210003. D.S. was supported by JSPS KAKENHI 19KK0082.

Appendix Light-curve Models without Parallax with Original and New MOA Photometry

An early version of this paper noted that the central value of the Einstein radius crossing resulting from our image-constrained modeling using the `eessunhong` code ($t_E = 55.8 \pm 5.5$ days) is $\sim 30\sigma$ larger than the best-fit value of $t_E = 42.46 \pm 0.45$ days quoted in the discovery paper (Suzuki et al. 2014a, 2014b) for the close model that has a smaller χ^2 value than the wide model). The original version of this paper attributed this to the fact that the analysis in the discovery paper did not include microlensing parallax. Microlensing parallax was included in the initial modeling efforts for this event, but because the source is faint, the odds of detecting a real microlensing parallax signal were small. The initial analysis did find a formally significant microlensing parallax signal, with a very large amplitude that was considered too large to be physical. When the light curve is only sensitive to very large microlensing parallax amplitudes, it is common for the modeling code to identify modest bumps in the light curve as being caused by a second approach to the lens. This is because the projected lens–source relative motion is not much larger than the Earth’s orbital velocity when the microlensing parallax amplitude is large. This occurs regularly when the data do not even constrain the microlensing parallax signals to reasonable values, because the modeling code can probe a large fraction of the light curve for false parallax signals due to rare systematic photometry errors. Suzuki et al. (2014a, 2014b) took the most common approach when microlensing parallax modeling seems to favor an implausibly large signal caused by systematic photometry errors. They simply avoided this problem by not including microlensing parallax in the model.

This approach can also be justified by an appeal to Occam’s razor, which is often paraphrased as the statement that “the simplest explanation is usually the best one.” This Occam’s razor approach is sensible if one is trying to demonstrate that a specific effect, like microlensing parallax or planetary orbital motion, has been detected by the light-curve photometry. However, we know the microlensing parallax effect must exist for Galactic microlensing events observed from a telescope that is being accelerated by the Sun’s gravitational field. Models without microlensing parallax usually yield solutions with physically reasonable parameters, with one glaring exception: it is unphysical to set $\pi_E \equiv 0$ if the observations were done with a telescope in orbit about the Sun. In many cases, setting $\pi_E \equiv 0$ will have no practical effect. However, it is not uncommon for this $\pi_E \equiv 0$ constraint to restrict other light-curve parameters, and these restrictions can exclude the correct models. This problem with setting $\pi_E \equiv 0$ is evident for three microlensing events out of 28 in the Suzuki et al. (2016) statistical sample. The t_E values for microlensing parallax models differ from the values with $\pi_E \equiv 0$ by 17σ , 12σ , and 6.3σ for OGLE-2007-BLG-368 (Sumi et al. 2010), MOA-2009-BLG-387 (Batista et al. 2011), and OGLE-2012-BLG-0563 (Fukui et al. 2015), respectively.


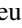







A more detailed examination of this issue indicates that the $\pi_E \equiv 0$ is not responsible for the small t_E uncertainty reported in Suzuki et al. (2014a, 2014b). We have remodeled the 2013 photometry used in the discovery with the modeling code used

Table 5
Close Separation Models with no Microlensing Parallax

Parameter	2013 MOA Photometry			2018 MOA phot. eesunhong
	S14	S14-new	eesunhong	
t_E (days)	42.46 ± 0.45	42.46 ± 4.93	40.50 ± 6.03	46.57 ± 5.93
t_0 (HJD ⁰)	4687.897 ± 0.001	4687.897 ± 0.001	4687.8937 ± 0.0019	4687.8950 ± 0.0009
$u_0 \times 10^3$	6.02 ± 0.06	6.02 ± 0.73	6.59 ± 1.05	5.64 ± 0.79
s	0.903 ± 0.001	0.903 ± 0.002	0.952 ± 0.011	0.932 ± 0.008
α (rad)	1.129 ± 0.002	1.129 ± 0.004	1.1329 ± 0.0035	1.1351 ± 0.0021
$q \times 10^3$	6.85 ± 0.05	6.85 ± 0.81	7.04 ± 1.02	6.22 ± 0.78
t_* (days)	0.0212 ± 0.0020	0.021 ± 0.003	0.0208 ± 0.0027	0.0216 ± 0.0030
fit χ^2	1246.0	1246.0	1242.80	1289.96
dof	~ 1239	~ 1239	~ 1238	~ 1274

in the discovery paper and with the `eesunhong` code, and the results are compared to the results reported by Suzuki et al. (2014a, 2014b) in Table 5 for the close solutions. The best-fit models using the code used by Suzuki et al. (2014a, 2014b) are identical, but the error bars are larger for the new reduction (labeled S14-new) because the new MCMC runs were run long enough to converge. The modeling of the 2013 data with the `eesunhong` code yields slightly different results due to slightly different treatment of the photometry error bar estimates. The last column of Table 5 shows the no-parallax modeling results from the `eesunhong` code using the 2018 MOA photometry, which has systematic errors due to color-dependent atmospheric refraction effects with a detrending method (Bennett et al. 2012; Bond et al. 2017). Systematic errors due to atmospheric refraction effects are known to have an annual correlation that can lead to erroneous microlensing parallax measurements (Terry et al. 2024). Table 5 shows only the close model parameters, but a comparison of the wide models yields nearly identical results. The analysis of using the 2013 MOA photometry with the `eesunhong` modeling code excluded one observation from the baseline as an outlier. Note that the error bars from the original analysis (labeled S14) are about an order of magnitude too small for all model parameters except for t_0 and t_* . The reason for this is probably the fact that these parameters are less affected by the blending degeneracy (Yee et al. 2012). Evidently, the blending degeneracy was not effectively probed by the original MCMC analysis.

ORCID iDs

David P. Bennett  <https://orcid.org/0000-0001-8043-8413>
 Jean-Philippe Beaulieu  <https://orcid.org/0000-0003-0014-3354>
 Naoki Koshimoto  <https://orcid.org/0000-0003-2302-9562>
 Joshua W. Blackman  <https://orcid.org/0000-0001-5860-1157>
 Clément Ranc  <https://orcid.org/0000-0003-2388-4534>
 Sean K. Terry  <https://orcid.org/0000-0002-5029-3257>
 Jessica R. Lu  <https://orcid.org/0000-0001-9611-0009>
 Greg Olmschenk  <https://orcid.org/0000-0001-8472-2219>
 Daisuke Suzuki  <https://orcid.org/0000-0002-5843-9433>

References

Adams, F. C., Meyer, M. R., & Adams, A. D. 2021, *ApJ*, 909, 1
 Adams, A. D., Boyajian, T. S., & von Braun, K. 2018, *MNRAS*, 473, 3608
 Alard, C. 1997, *A&A*, 321, 424
 Alcock, C., Akerlof, C. W., Allsman, R. A., et al. 1993, *Natur*, 365, 621
 Alcock, C., Allsman, R. A., Alves, D., et al. 1995, *ApJL*, 454, L125

Ali-Dib, M., Cumming, A., & Lin, D. N. C. 2022, *MNRAS*, 509, 1413
 Bachelet, E., Fouqué, P., Han, C., et al. 2012, *A&A*, 547, A55
 Batista, V., Gould, A., Dieters, S., et al. 2011, *A&A*, 529, A102
 Batista, V., Beaulieu, J.-P., Gould, A., et al. 2014, *ApJ*, 780, 54
 Batista, V., Beaulieu, J.-P., Bennett, D. P., et al. 2015, *ApJ*, 808, 170
 Beaulieu, J.-P. 2018, *Univ*, 4, 61
 Beaulieu, J.-P., Bennett, D. P., Fouqué, P., et al. 2006, *Natur*, 439, 437
 Beaulieu, J.-P., Bennett, D. P., Batista, V., et al. 2016, *ApJ*, 824, 83
 Bennett, D. P. 2008, in *Exoplanets*, ed. J. Mason (Berlin: Springer)
 Bennett, D. P. 2010, *ApJ*, 716, 1408
 Bennett, D. 2019, Keck Observatory Archive N021, 117
 Bennett, D. P. 2014, *BAAS*, 46, 008
 Bennett, D. P., Akesson, R., Anderson, J., et al. 2018a, arXiv:1803.08564
 Bennett, D. P., Anderson, J., Beaulieu, J.-P., et al. 2010a, arXiv:1012.4486
 Bennett, D. P., Anderson, J., Bond, I. A., Udalski, A., & Gould, A. 2006, *ApJL*, 647, L171
 Bennett, D. P., Anderson, J., & Gaudi, B. S. 2007, *ApJ*, 660, 781
 Bennett, D. P., Batista, V., Bond, I. A., et al. 2014, *ApJ*, 785, 155
 Bennett, D. P., Bhattacharya, A., Anderson, J., et al. 2015, *ApJ*, 808, 169
 Bennett, D. P., Bhattacharya, A., Beaulieu, J.-P., et al. 2020, *AJ*, 159, 68
 Bennett, D. P., Bond, I. A., Udalski, A., et al. 2008, *ApJ*, 684, 663
 Bennett, D. P., & Khavinson, D. 2014, *PhT*, 67, 64
 Bennett, D. P., Ranc, C., & Fernandes, R. B. 2021, *AJ*, 162, 243
 Bennett, D. P., & Rhie, S. H. 1996, *ApJ*, 472, 660
 Bennett, D. P., & Rhie, S. H. 2002, *ApJ*, 574, 985
 Bennett, D. P., Rhie, S. H., Nikolaev, S., et al. 2010b, *ApJ*, 713, 837
 Bennett, D. P., Rhie, S. H., Udalski, A., et al. 2016, *AJ*, 152, 125
 Bennett, D. P., Sumi, T., Bond, I. A., et al. 2012, *ApJ*, 757, 119
 Bennett, D. P., Udalski, A., Han, C., et al. 2018, *AJ*, 155, 141
 Bertin, E., & Arnouts, S. 1996, *A&AS*, 117, 393
 Bertin, E., Mellier, Y., Radovich, M., et al. 2002, *ASP Conf. Ser.* 281, The TERAPIX Pipeline (San Francisco, CA: ASP), 228
 Bhattacharya, A., Bennett, D. P., Anderson, J., et al. 2017, *AJ*, 154, 59
 Bhattacharya, A., Beaulieu, J.-P., Bennett, D. P., et al. 2018, *AJ*, 156, 289
 Bhattacharya, A., Bennett, D. P., Beaulieu, J. P., et al. 2021, *AJ*, 162, 60
 Blackman, J. W., Beaulieu, J. P., Bennett, D. P., et al. 2021, *Natur*, 598, 272
 Bond, I. A., Abe, F., Dodd, R. J., et al. 2001, *MNRAS*, 327, 868
 Bond, I. A., Bennett, D. P., Sumi, T., et al. 2017, *MNRAS*, 469, 2434
 Bond, I. A., Udalski, A., & Jaroszyński, M. 2004, *ApJL*, 606, L155
 Boyajian, T. S., van Belle, G., & von Braun, K. 2014, *AJ*, 147, 47
 Cassan, A., Kubas, D., Beaulieu, J.-P., et al. 2012, *Natur*, 481, 167
 Childs, A. C., Martin, R. G., & Livio, M. 2022, *ApJL*, 937, L41
 Di Stefano, R., & Esin, A. A. 1995, *ApJL*, 448, L1
 Dominik, M. 1999, *A&A*, 349, 108
 Dominik, M., & Hirshfeld, A. C. 1994, *A&A*, 289, L31
 Dong, S., Bond, I. A., Gould, A., et al. 2009a, *ApJ*, 698, 1826
 Dong, S., Gould, A., Udalski, A., et al. 2009b, *ApJ*, 695, 970
 Drimmel, R., & Spergel, D. N. 2001, *ApJ*, 556, 181
 Emsenhuber, A., Mordasini, C., Burn, R., et al. 2021, *A&A*, 656, A70
 Fukui, A., Gould, A., Sumi, T., et al. 2015, *ApJ*, 809, 74
 Fulton, B. J., Rosenthal, L. J., Hirsch, L. A., et al. 2021, *ApJS*, 255, 14
 Furusawa, K., Udalski, A., Sumi, T., et al. 2013, *ApJ*, 779, 91
 Gaudi, B. S. 2012, *ARA&A*, 50, 411
 Gaudi, B. S., Bennett, D. P., Udalski, A., et al. 2008, *Sci*, 319, 927
 Gaudi, B. S., & Gould, A. 1997, *ApJ*, 486, 85
 Ghosh, H., DePoy, D. L., Gal-Yam, A., et al. 2004, *ApJ*, 615, 450
 Gould, A. 1992, *ApJ*, 392, 442
 Gould, A. 2014, *J. Kor. Ast. Soc.*, 47, 215

- Gould, A., Dong, S., Gaudi, B. S., et al. 2010, *ApJ*, 720, 1073
- Gould, A., & Loeb, A. 1992, *ApJ*, 396, 104
- Gould, A., Miralda-Escude, J., & Bahcall, J. N. 1994, *ApJL*, 423, L105
- Gould, A., Udalski, A., An, D., et al. 2006, *ApJL*, 644, L37
- Gould, A., Udalski, A., Monard, B., et al. 2009, *ApJL*, 698, L147
- Grazier, K. R. 2016, *AsBio*, 16, 23
- Griest, K., & Safizadeh, N. 1998, *ApJ*, 500, 37
- Han, C., Bennett, D. P., Udalski, A., & Jung, Y. K. 2016, *ApJ*, 825, 8
- Holtzman, J. A., Watson, A. M., Baum, W. A., et al. 1998, *AJ*, 115, 1946
- Ida, S., & Lin, D. N. C. 2004, *ApJ*, 604, 388
- Janczak, J., Fukui, A., Dong, S., et al. 2010, *ApJ*, 711, 731
- Johnson, S. A., Penny, M., Gaudi, B. S., et al. 2020, *AJ*, 160, 123
- Kervella, P., Thévenin, F., Di Folco, E., & Ségransan, D. 2004, *A&A*, 426, 297
- Koshimoto, N., Baba, J., & Bennett, D. P. 2021a, *ApJ*, 917, 78
- Koshimoto, N., Bennett, D. P., & Suzuki, D. 2020, *AJ*, 159, 268
- Koshimoto, N., Bennett, D. P., Suzuki, D., et al. 2021b, *ApJL*, 918, L8
- Laughlin, G., Bodenheimer, P., & Adams, F. C. 2004, *ApJL*, 612, L73
- Lecavelier des Etangs, & Lissauer, J. J. 2022, *NewAR*, 94, 101641
- Lissauer, J. J. 1993, *ARA&A*, 31, 129
- Lu, J. R. 2008, PhD thesis, UCLA
- Lu, J. 2022, Keck-Data Reduction Pipelines/KAI: v1.0.0 Release of KAI (v1.0.0). Zenodo, [10.5281/zenodo.6522913](https://doi.org/10.5281/zenodo.6522913)
- Mao, S., & Paczynski, B. 1991, *ApJL*, 374, L37
- Mayor, M., Marmier, M., Lovis, C., et al. 2011, arXiv:1109.2497
- Minniti, D., Lucas, P. W., Emerson, J. P., et al. 2010, *NewA*, 15, 433
- Mulders, G. D., Pascucci, I., & Apai, D. 2015, *ApJ*, 798, 112
- Mordasini, C., Alibert, Y., & Benz, W. 2009, *A&A*, 501, 1139
- Muraki, Y., Han, C., Bennett, D. P., et al. 2011, *ApJ*, 741, 22
- Nataf, D. M., Gould, A., Fouqué, P., et al. 2013, *ApJ*, 769, 88
- Nayakshin, S., Dipierro, G., & Szulágyi, J. 2019, *MNRAS*, 488, L12
- Nayakshin, S., Elbakyan, V., & Rosotti, G. 2022, *MNRAS*, 512, 6038
- Nishiyama, S., Nagata, T., Kusakabe, N., et al. 2006, *ApJ*, 638, 839
- Osinski, G. R., Cockell, C. S., Pontefract, A., et al. 2020, *AsBio*, 20, 1121
- Penny, M. T., Gaudi, B. S., Kerins, E., et al. 2019, *ApJS*, 241, 3
- Penny, M. T., Henderson, C. B., & Clanton, C. 2016, *ApJ*, 830, 150
- Poleski, R., Udalski, A., Dong, S., et al. 2014, *ApJ*, 782, 47
- Pollack, J. B., Hubickyj, O., Bodenheimer, P., et al. 1996, *Icar*, 124, 62
- Poindexter, S., Afonso, C., Bennett, D. P., et al. 2005, *ApJ*, 633, 914
- Quenouille, M. H. 1949, *Ann. Math. Stat.*, 20, 355
- Quenouille, M. H. 1956, *Biometrika*, 43, 353
- Raymond, S. N., Quinn, T., & Lunine, J. I. 2004, *Icar*, 168, 1
- Raymond, S. N., Quinn, T., & Lunine, J. I. 2007, *AsBio*, 7, 66
- Rhie, S. H., Becker, A. C., Bennett, D. P., et al. 1999, *ApJ*, 522, 1037
- Rhie, S. H., & Bennett, D. P. 1996, *NuPhS*, Vol. 51, 86
- Rhie, S. H., Bennett, D. P., Becker, A. C., et al. 2000, *ApJ*, 533, 378
- Rosenthal, L. J., Fulton, B. J., Hirsch, L. A., et al. 2021, *ApJS*, 255, 8
- Schlecker, M., Burn, R., Sabotta, S., et al. 2022, *A&A*, 664, A180
- Shin, I.-G., Han, C., Choi, J.-Y., et al. 2015, *ApJ*, 802, 108
- Sinclair, C. A., Wyatt, M. C., Morbidelli, A., et al. 2020, *MNRAS*, 499, 5334
- Skowron, J., Shin, I.-G., Udalski, A., et al. 2015, *ApJ*, 804, 33
- Spergel, D., Gehrels, N., Baltay, C., et al. 2015, arXiv:1503.03757
- Stetson, P. B. 1987, *PASP*, 99, 191S
- Sumi, T., Bennett, D. P., Bond, I. A., et al. 2010, *ApJ*, 710, 1641
- Sumi, T., Udalski, A., Bennett, D. P., et al. 2016, *ApJ*, 825, 112
- Surot, F., Valenti, E., Gonzalez, O. A., et al. 2020, *A&A*, 644, A140
- Suzuki, D., Bennett, D. P., Ida, S., et al. 2018, *ApJL*, 869, L34
- Suzuki, D., Bennett, D. P., Sumi, T., et al. 2016, *ApJ*, 833, 145
- Suzuki, D., Udalski, A., Sumi, T., et al. 2014a, *ApJ*, 780, 123
- Suzuki, D., Udalski, A., Sumi, T., et al. 2014b, *ApJ*, 788, 97
- Szulágyi, J., Morbidelli, A., Crida, A., et al. 2014, *ApJ*, 782, 65
- Szymański, M. K., Udalski, A., Soszyński, I., et al. 2011, *AcA*, 61, 83
- Terry, S. K., Beaulieu, J.-P., Bennett, D. P., et al. 2024, arXiv:2403.12118
- Terry, S. K., Bennett, D. P., Bhattacharya, A., et al. 2022, *AJ*, 164, 217
- Terry, S. K., Bhattacharya, A., Bennett, D. P., et al. 2021, *AJ*, 161, 54
- Tierney, L., & Mira, A. 1999, *Stat. Med.*, 18, 2507
- Thompson, S. E., Coughlin, J. L., Hoffman, K., et al. 2018, *ApJS*, 235, 38
- Tsapras, Y., Choi, J.-Y., Street, R. A., et al. 2014, *ApJ*, 782, 48
- Tukey, J. W. 1958, *Ann. Math. Stat.*, 29, 614
- Udalski, A., Jaroszyński, M., Paczyński, B., et al. 2005, *ApJL*, 628, L109
- Udalski, A., Szymański, M., Kałużny, J., et al. 1994, *AcA*, 44, 227
- Udalski, A., Yee, J. C., Gould, A., et al. 2015, *ApJ*, 799, 237
- Vandorou, A., Bennett, D. P., Beaulieu, J.-P., et al. 2020, *AJ*, 160, 121
- Yee, J. C., Shvartzvald, Y., Gal-Yam, A., et al. 2012, *ApJ*, 755, 102
- Zhang, K., Gaudi, B. S., & Bloom, J. S. 2022, *NatAs*, 6, 782